

THE ATACAMA COSMOLOGY TELESCOPE: DR6 SUNYAEV-ZEL'DOVICH SELECTED GALAXY CLUSTERS CATALOG

M. AGUENA^{1,2}, S. AIOLA^{3,4}, S. ALLAM⁵, F. ANDRADE-OLIVEIRA⁶, D. BACON⁷, N. BAHCALL⁸, N. BATTAGLIA⁹, E. S. BATTISTELLI¹⁰, S. BOCQUET¹¹, B. BOLLIET^{12,13}, J. R. BOND¹⁴, D. BROOKS¹⁵, E. CALABRESE¹⁶, J. CARRETERO¹⁷, S. K. CHOI¹⁸, L. N. DA COSTA², M. COSTANZI^{19,1,20}, W. COULTON^{13,21}, T. M. DAVIS²², S. DESAI²³, M. J. DEVLIN²⁴, S. DICKER²⁴, P. DOEL¹⁵, A. J. DUIVENVOORDEN²⁵, J. DUNKLEY^{4,26}, S. FERRARO^{27,28,29}, B. FLAUGHER⁵, J. FRIEMAN^{30,5,31}, P. A. GALLARDO²⁴, M. GATTI³¹, E. GAZTANAGA^{32,7,33}, A. S. GILL³⁴, J. E. GOLEC³⁵, D. GRUEN¹¹, R. A. GRUENDL^{36,37}, M. HALPERN³⁸, M. HASSELFIELD³, J. C. HILL^{39,3}, M. HILTON^{40,41*}, A. D. HINCKS^{42,43}, S. R. HINTON²², D. L. HOLLOWOOD⁴⁴, K. HONSCHEID^{45,46}, J. HUBMAYR⁴⁷, K. M. HUFFENBERGER⁴⁸, J. P. HUGHES⁴⁹, D. J. JAMES⁵⁰, M. KLEIN¹¹, K. KNOWLES⁵¹, B. J. KOOPMAN⁵², A. KOSOWSKY⁵³, O. LAHAV¹⁵, E. LEE²⁴, Y. LIN⁵⁴, M. LOKKEN⁵⁵, M. S. MADHAVACHERIL²⁴, A. A. PLAZAS MALAGÓN^{56,57}, J. v. MARREWILK⁵⁸, J. L. MARSHALL⁵⁹, J. MCMAHON^{60,61,35,62}, J. MENA-FERNÁNDEZ⁶³, R. MIQUEL^{64,17}, H. MIYATAKE^{65,66,67}, J. J. MOHR¹¹, K. MOODLEY⁴¹, T. MROCKOWSKI⁶⁸, S. NAESS⁶⁹, F. NATI⁷⁰, A. NICOLA⁷¹, M. D. NIEMACK^{72,9}, R. L. C. OGANDO^{73,74}, M. OGURI^{75,76}, J. ORLOWSKI-SCHERER²⁴, L. A. PAGE⁴, B. PARTRIDGE⁷⁷, M. E. DA SILVA PEREIRA⁷⁸, A. PORREDON^{79,80}, F. J. QU^{81,82}, D. C. RAGAVAN⁴⁰, B. RIED GUACHALLA^{81,82,83}, A. K. ROMER⁸⁴, A. CARNERO ROSELL^{85,2,86}, E. S. RYKOFF^{56,57}, S. SAMUROFF^{87,17}, E. SANCHEZ⁷⁹, I. SEVILLA-NOARBE⁷⁹, C. SIERRA³⁵, C. SIFÓN⁸⁸, M. SMITH⁸⁹, S. T. STAGGS⁴, E. SUCHYTA⁹⁰, M. E. C. SWANSON³⁶, D. L. TUCKER⁵, C. VARGAS⁴⁸, E. M. VAVAGIAKIS^{91,72}, J. DE VICENTE⁷⁹, N. WEAVERDYCK^{92,93}, J. WELLER^{94,95}, E. J. WOLLACK⁹⁶, AND I. ZUBELDIA^{97,13}

(Affiliations can be found after the references)

(ACT-DES-HSC COLLABORATION)

Version January 27, 2026

ABSTRACT

We present the results of a search for galaxy clusters in the Atacama Cosmology Telescope (ACT) Data Release 6 (DR6) microwave sky maps covering 16293 square degrees in three frequency bands, using data obtained over the lifetime of the project (2008–2022). We report redshifts and mass estimates for 10040 clusters detected via their Sunyaev-Zel'dovich (SZ) effect with signal-to-noise greater than 4 at a 2.4 arcminute filter scale. The catalog includes 1180 clusters at redshifts greater than 1, and 124 clusters at redshifts greater than 1.5. Using a relation between cluster SZ signal and mass that is consistent with recent weak-lensing measurements, we estimate that clusters detected with signal-to-noise greater than 5 form a sample which is 90% complete for clusters with masses greater than $5 \times 10^{14} M_{\odot}$ (measured within a spherical volume with mean density 500 times the critical density). El Gordo, a cluster found in an initial ACT survey of 755 square degrees, remains the most extreme cluster in mass and redshift; we find no cluster with a mass and redshift combination high enough to falsify the standard Λ CDM cosmology with Gaussian initial perturbations. We make public a variety of data products, including the full cluster candidate list, noise maps, and sky masks, along with our software for cluster detection and instructions for reproducing our cluster catalogs from the public ACT maps.

1. INTRODUCTION

Over the past two decades, the development of increasingly sensitive millimeter wavelength instruments, capable of surveying large areas of the sky with arcminute resolution, has progressed significantly. These advancements have enabled the detection of massive galaxy clusters spanning the last 10 Gyr of cosmic history by exploiting the thermal Sunyaev-Zel'dovich effect (SZ; Sunyaev & Zel'dovich 1970; Sunyaev & Zeldovich 1972).

The SZ effect is the inverse Compton scattering of cosmic microwave background (CMB) photons by electrons in the hot gaseous atmospheres of galaxy clusters (see reviews by Birkinshaw 1999; Carlstrom et al. 2002; Mroczkowski et al. 2019). The SZ signal, which is in principle unaffected by the distance to the observer, provides a measure of the integrated thermal pressure along the line of sight. This correlates with the total mass of clusters, allowing SZ surveys to construct approximately mass-limited cluster samples with unlimited

redshift reach. One application of such catalogs is to constrain cosmological parameters using the evolution of cluster number counts, with the current state-of-the-art represented by the Bocquet et al. (2024) analysis of 1005 SZ-selected clusters detected by the South Pole Telescope (SPT).

Thousands of clusters, reaching up to $z = 2$, have now been detected using blind SZ surveys by ACT (Marriage et al. 2011; Hasselfield et al. 2013; Hilton et al. 2018, 2021), *Planck* (Planck Collaboration et al. 2014, 2016b; Zubeldia et al. 2025), and SPT (Staniszewski et al. 2009; Williamson et al. 2011; Bleem et al. 2015, 2020; Huang et al. 2020; Bleem et al. 2024; Klein et al. 2024b; Archipley et al. 2025). The majority of these have been found using ACT data (Hilton et al. 2021; Klein et al. 2024a), due to a combination of the sensitivity of the AdvACT receiver (Henderson et al. 2016; Choi et al. 2018), and the fact that ACT observed one-third of the extragalactic sky (Naess et al. 2020). The deepest observations, detecting the lowest mass SZ-selected clusters to date ($M_{500c} \approx 1.5 \times 10^{14} M_{\odot}$), have been performed by SPT

*E-mail: matt.hilton@wits.ac.za

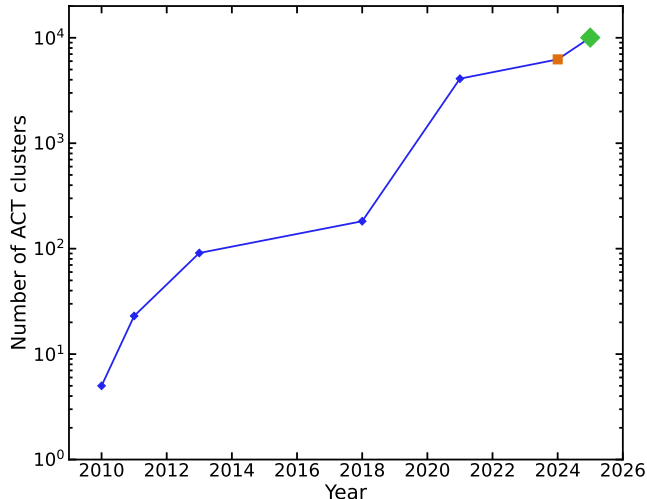


Figure 1. The number of ACT-detected SZ-selected clusters reported over the lifetime of the project. References for the blue points: First detections (Hincks et al. 2010); ACT DR1 (Marriage et al. 2011; Menanteau et al. 2010); ACT DR2 (Hasselfield et al. 2013; Menanteau et al. 2013a); ACT DR3 (Hilton et al. 2018); ACT DR5 (Hilton et al. 2021). The orange square marks the ACT-DR5 MCMF catalog (Klein et al. 2024a), which is based on an independent re-run of the NEMO software on the ACT DR5 maps, followed by optical confirmation using the DESI Legacy Imaging Surveys DR10 (Dey et al. 2019). The green diamond marks the 10040 clusters reported in the current work, based on the ACT DR6 maps, which is > 1.5 times larger than catalogs produced using ACT DR5 data.

(Bleem et al. 2024; Kornoelje et al. 2025).

In this paper we report on a search for SZ clusters in the ACT Data Release 6 (DR6) maps (Naess et al. 2025), using data collected from 2008 to 2022. Figure 1 illustrates how the number of SZ clusters detected by ACT has grown with each data release. Together with this paper, we release a number of data products related to the cluster search.¹ This includes a catalog of 10040 clusters with mass and redshift estimates detected across the maximum 16293 deg^2 search area (see Table A3 for a description of the contents and a list of symbols used in this paper); a complete, high signal-to-noise subsample of 3747 clusters over a 10317 deg^2 area that we refer to as the ‘Legacy sample’, which is suggested for cosmological analyses; the full list of 21558 cluster candidates (i.e., including objects without redshift estimates and optical confirmation); and various files related to the cluster selection (masks, flagged areas, random catalogs, and noise properties as a function of sky position). The top panel of Figure 2 shows the location of the ACT DR6 cluster search area compared with the footprints of several other surveys on the sky. The bottom panel of Figure 2 shows the location of the optically confirmed SZ-detected clusters reported in this work, highlighting in particular the Legacy sample.

This paper is organized as follows. In Section 2 we describe the ACT maps, detection of cluster candidates, and mass completeness estimates, highlighting differences with respect to the previous analysis based on ACT DR5. In Section 3 we explain the process of obtaining redshift estimates for the cluster candidates. In

Section 4, we describe the ACT DR6 cluster search data products, and present the properties of the cluster catalog. We discuss how the DR6 sample compares to the ACT DR5 and SRG/eROSITA (Sunyaev et al. 2021) All-Sky Survey (eRASS1 Western Galactic hemisphere; Bulbul et al. 2024) cluster catalogs in Section 5. We summarize our findings in Section 6.

We assume a flat Λ CDM cosmology with $\Omega_m = 0.3$, $\Omega_\Lambda = 0.7$, and $H_0 = 70 \text{ km s}^{-1} \text{ Mpc}^{-1}$ throughout. We report cluster mass estimates ($M_{\Delta c}$) within a spherical radius that encloses an average density equal to Δ times the critical density at the cluster redshift ($R_{\Delta c}$), where $\Delta = 200$ or 500 . We replace the subscript c with subscript m to indicate a mass estimate with respect to Δ times the mean density of the Universe at the cluster redshift. Note that the mass calibration adopted in this paper differs from that used in previous ACT cluster catalogs (see Section 2.5 for details).

2. ACT OBSERVATIONS AND SZ CLUSTER DETECTION

2.1. Observations and Maps

ACT observed the millimeter sky from Chile with arcminute resolution from 2007² to 2022, using three generations of receivers: the Millimeter Bolometer Array Camera (MBAC; Swetz et al. 2011, 2007–2011); ACTPol (Thornton et al. 2016, 2013–2016); and AdvACT (Henderson et al. 2016; Choi et al. 2018, 2016–2022). In this work we use maps covering three frequency bands named f090, f150, and f220, where the number indicates the approximate center of the observed frequency range in GHz. These have angular resolutions of $2.1'$, $1.4'$, and $1.0'$ respectively. To maximize our sensitivity to the SZ signal, we use the deepest available ACT data, which are the co-added maps from ACT DR6 that include all usable daytime and nighttime data (Naess et al. 2025). The method used to create these co-added maps is described in detail in Naess et al. (2020). We use the DR6 release ACT+Planck day+night coadds with ACT DR4 data included, which therefore includes observations from 2008 to 2022. These cover approximately 19000 deg^2 .

2.2. Cluster Finding

We use the NEMO³ package for SZ cluster detection and much of the subsequent analysis presented in this work. Earlier versions of NEMO were used for the ACT DR3 (Hilton et al. 2018) and ACT DR5 (Hilton et al. 2021, H21 hereafter) cluster searches. Cluster candidates are identified by using a multi-frequency matched filter (e.g., Melin et al. 2006; Williamson et al. 2011),

$$\psi(k_x, k_y, \nu_i) = A \sum_j \mathbf{N}_{ij}^{-1}(k_x, k_y) f_{\text{SZ}}(\nu_j) S(k_x, k_y, \nu_j), \quad (1)$$

where ψ is the filter, (k_x, k_y) denote the spatial frequencies in the horizontal and vertical directions in the maps, \mathbf{N} is the noise covariance between the maps at different frequencies ν , S is a beam-convolved signal template,

² The telescope saw first light in 2007; in this paper we use data from 2008 onwards.

³ <https://github.com/simonsobs/nemo/>; see <https://nemo-sz.readthedocs.io> for documentation, including a tutorial on how to reproduce the cluster search data products described in this paper.

¹ All data products are available from LAMBDA: https://lambda.gsfc.nasa.gov/product/act/actadv_prod_table.html

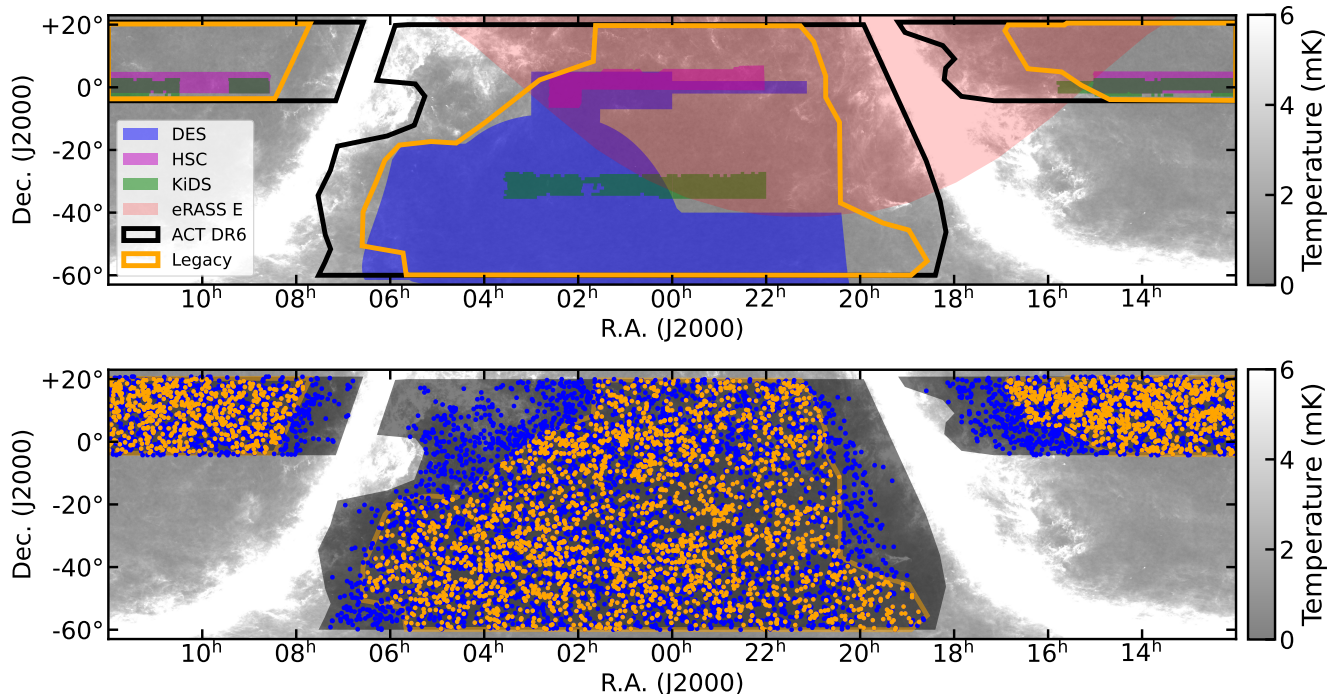


Figure 2. Top panel: The full ACT DR6 cluster search region (black outline), covering 16293 deg^2 before masking. The orange outline shows the 10317 deg^2 Legacy footprint (after masking and flagging) used to define the ‘Legacy sample’ (see Section 4). The footprints of deep and wide optical surveys are highlighted, with the overlapping area with ACT DR6 (after masking and flagging) given in square degrees: DES (blue; [Abbott et al. 2021](#); 4391 deg^2); HSC (magenta; [Aihara et al. 2022](#); 1078 deg^2); and KiDS (green; [Wright et al. 2024](#); 802 deg^2). The red shaded region indicates the region of sky covered by the Russian half of the eROSITA survey; the rest of the ACT search area has 7044 deg^2 of overlap with the German half of the eROSITA sky ([Merloni et al. 2024](#)). Bottom panel: Blue points mark the locations of 10040 optically confirmed SZ-detected clusters reported in this paper. The ‘Legacy sample’ of 3747 clusters detected at signal-to-noise $\tilde{q} > 5.5$ are marked with orange points. The full ACT search area is shown by the dark gray shaded region. In both panels, the *Planck* 353 GHz map is shown in the background, to highlight regions of sky that have more thermal emission from dust.

and A is a normalization factor. When applied to a set of maps containing a beam-convolved cluster signal (in temperature units), A is chosen such that the matched filter returns the central Comptonization parameter (see Section 2.5 below), and f_{SZ} is the non-relativistic form for the spectral dependence of the SZ effect,

$$f_{\text{SZ}} = x \frac{e^x + 1}{e^x - 1} - 4, \quad (2)$$

where $x = h\nu/k_B T_{\text{CMB}}$ (the relativistic SZ suppresses the SZ signal for very high temperatures; we apply a correction for this when inferring cluster masses, as noted in Section 2.5 below). As in previous ACT cluster searches, we use the map itself to form the noise covariance \mathbf{N} , as the maps are dominated by the CMB on large scales, and white noise on small scales, rather than by the thermal SZ signal.

When filtering the map across multiple angular scales during the cluster search, we adopt the maximum S/N across all filter scales for each candidate as the ‘optimal’ S/N detection, for which we use the symbol q throughout this paper. However, as in previous ACT work, to mitigate inter-filter noise bias ([Hasselfield et al. 2013](#), H13 hereafter; see also the discussion of optimization bias in Appendix B), we use the S/N measured at a single reference filter scale ($\theta_{500c} = 2.4'$ as in H21; $\theta_{500c} = R_{500c}/D_A$, where D_A is the angular diameter distance), for which we use the symbol \tilde{q} . Similarly, we use the symbol \tilde{q}_0 to refer to the central Comptonization parameter, which is our adopted measurement of the SZ

signal (see Section 2.5).

Below we describe the improvements made for the DR6 cluster search compared to the ACT DR5 analysis.

2.2.1. Cluster Search Area and Tiling

We use a more extended cluster search area mask compared to DR5, extending to lower Galactic latitudes. This is shown as the black outline in the top panel of Figure 2, and covers a sky area of 16293 deg^2 . This allows us to identify cluster candidates in dusty regions that may have been missed by previous surveys, although in practice we flag such areas when constructing statistical cluster samples for cosmological analyses (see Section 2.2.3).

For efficiency, NEMO breaks up the ACT maps into tiles, which are processed separately (each with its own, different matched filter) and subsequently combined (see H21). Figure 3 shows the tiling arrangement chosen for the DR6 analysis. We have chosen to use tiles that nominally cover $25 \text{ deg} \times 2 \text{ deg}$ (right ascension \times declination). These are thinner than the $10 \text{ deg} \times 5 \text{ deg}$ tiles used in H21. This change was made due to a concern that the flat sky approximation, combined with the variable pixel scale due to the plate carrée projection (CAR in the terminology of Flexible Image Transport System (FITS) world coordinate systems; [Calabretta & Greisen 2002](#)), may introduce a small bias in cluster detection efficiency at high declination. Simulations have shown that this is not a problem for the $25 \text{ deg} \times 2 \text{ deg}$ tiling used in DR6 (see Appendix B, which presents the results of applying NEMO to simulated maps). As in H21, noise differences within

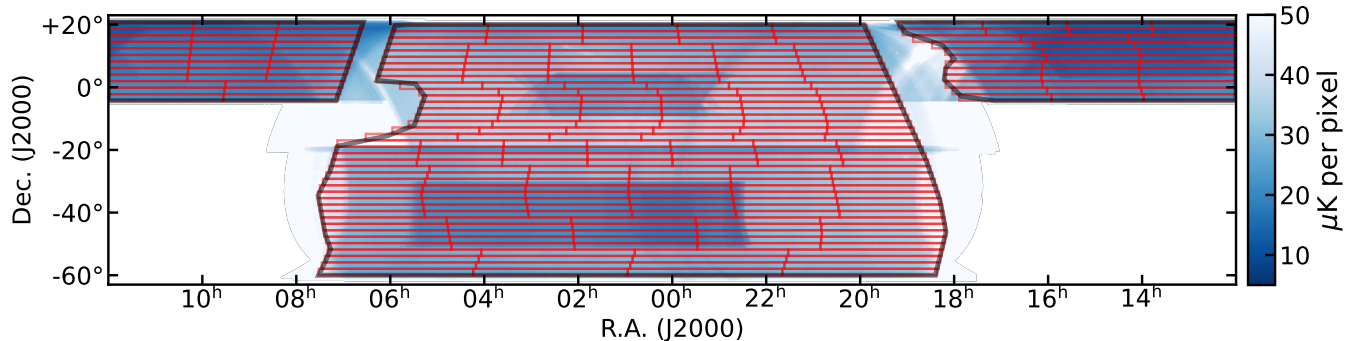


Figure 3. A map illustrating the tiling geometry chosen for the ACT DR6 cluster search. The red boxes indicate the locations of tiles, of nominal size $25 \text{ deg} \times 2 \text{ deg}$, that are processed independently by the cluster finder (see Section 2.2.1). The full 16293 deg^2 cluster search area (before masking and flagging) is shown as the black outline. The map in the background shows the variation in the white noise level as a function of position in the ACT+Planck day+night f090 map.

a tile are handled by making noise estimates within cells in the filtered maps (here we use cells that are nominally $80'$ on a side, with the exact size depending on the tile geometry).

2.2.2. Multi-pass Filtering and Object Detection

For the DR6 analysis, we make use of NEMO’s new multi-pass filtering and object detection feature, which was developed subsequent to the ACT DR5 release. This allows both point sources and clusters to be detected in a single run of the software. This multi-pass approach mitigates some signal loss which would occur if the cluster signal is not subtracted from the maps when estimating \mathbf{N} from the maps themselves. Zubeldia et al. (2023) describe a similar approach to the one used here, applied to *Planck* data. The procedure used for this work is as follows:

1. *Source detection run 1.* Detect $S/N > 50$ point sources by applying a matched filter with the signal template set to the appropriate ACT beam, for each of the f090, f150, and f220 maps individually (i.e., no spectral templates are used here).
2. *Source detection run 2.* Detect $S/N > 5$ point sources by applying a matched filter with the signal template set to the appropriate ACT beam, for each of the f090, f150, and f220 maps individually. Locations with sources detected in Step 1 are masked and in-filled with a median-filtered ($10'$ -scale) version of the map, when estimating \mathbf{N} in Equation (1).
3. *Initial cluster detection run.* Detect $q > 3$ clusters by applying a multi-frequency matched filter to the f090, f150, and f220 maps. Here, the Universal Pressure Profile (UPP; Arnaud et al. 2010) is used for the signal template, after convolution with the appropriate ACT beam. Detection is performed over 16 different angular scales, corresponding to UPP models with $M_{500c} \in \{(1, 2, 4, 8) \times 10^{14} M_{\odot}\}$ and $z \in \{0.2, 0.4, 0.8, 1.2\}$ (these are the same as in H21). Locations with sources detected in Step 1 are masked and in-filled as described in Step 2. Sources detected in Step 2 are subtracted from the maps, before estimating \mathbf{N} in Equation (1).
4. *Final cluster detection run.* Detect $\tilde{q} > 4$ clusters by applying a multi-frequency matched filter

to the f090, f150, and f220 maps, using the same filter scales as in Step 3. Before estimating \mathbf{N} in Equation (1), sources detected in Steps 1 and 2 are handled as described in Step 3. Cluster candidates detected in Step 3 are also subtracted before estimating \mathbf{N} , using the signal template with the maximum S/N for each detected cluster. We find that further passes are not necessary (i.e., do not result in the detection of additional cluster candidates).

We have also made some changes to how object detection is handled and how multi-scale catalogs are combined compared to H21. We now apply a 3σ threshold when constructing the object segmentation map⁴ and measuring object properties (position, q , \tilde{y}_0 , etc.), and then cut the catalog to the chosen $\tilde{q} > 4$ limit in the final step. This avoids incompleteness near the chosen $\tilde{q} > 4$ limit, as noted by Klein et al. (2024a), who re-ran NEMO to reproduce the H21 cluster candidate list.⁵ We also fixed a bug related to the minimum number of pixels required for object detection (in H21, the minimum number of pixels required for a detection was accidentally set to 2, rather than the intended 1 pixel, which means that the H21 catalog was purer than might have been expected at $q \approx 4$). Finally, object positions in DR6 are reported from the reference $2.4'$ filter scale map (see Section 2.5 below), rather than from the highest S/N object detection across all filter scales (in practice this change has little impact, but it was made for the purposes of minimizing optimization bias and calculating the correction for this consistently; see Appendix B). Fig. 4 shows the signal-to-noise (\tilde{q}) distribution close to the detection limit for the full candidate list.

2.2.3. Flagging

In H21, we took the approach of masking point sources, zeroing such regions of the filtered map. For the DR6

⁴ A segmentation map identifies which pixels in an image (the filtered map in our case) belong to which object in a catalog.

⁵ The `thresholdSigma` parameter in NEMO sets the S/N threshold used for constructing the segmentation map from which objects are identified. The segmentation map includes only pixels for which the S/N value is $> \text{thresholdSigma}$. So, if `thresholdSigma` is set to the same value as the desired S/N cut of the output catalog (as was done for the ACT DR5 release), the resulting catalog is incomplete at the S/N cut, because the sub-pixel interpolation routine cannot include pixels with S/N values just below the threshold. More details can be found in the NEMO documentation.

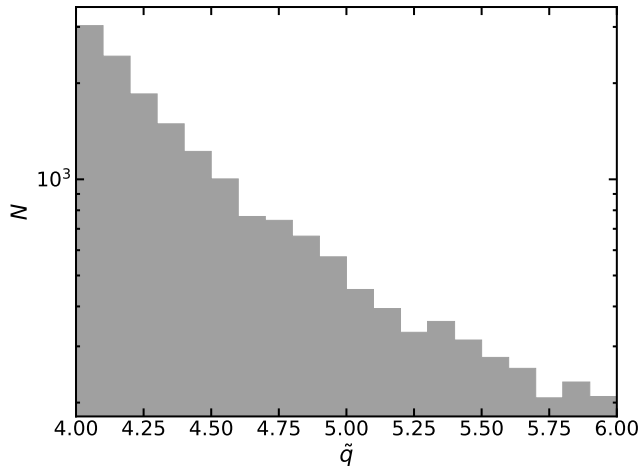


Figure 4. Distribution of signal-to-noise (\tilde{q}) values close to the detection limit for the full cluster candidate list. In our analysis, we make use of NEMO’s new flagging features instead. We produce a separate flag map (see Figure 5) that records pixels in the map that are potentially affected by any of the following issues:

1. *Point source subtraction.* Map pixels where a point source (found in Steps 1-2 in Section 2.2.2) was subtracted are flagged. These are considered independently across the f090, f150, and f220 maps, so a point source detected in all three frequencies will be flagged multiple times in the flag mask. The main motivation for subtracting and flagging, rather than masking, was to attempt to recover clusters affected by central point sources, but this was not successful (see Section 5.2). Objects affected by point source subtraction are indicated with a non-zero value for `finderFlag` in the cluster catalog (see Table A3).
2. *Dusty regions.* We identify dusty regions by thresholding the *Planck* 353 GHz map above 2 mK (this is more conservative than the 4 mK threshold used in H21). This threshold was chosen based on visual inspection of cluster candidates in dusty regions, where positive residuals, identified as spurious detections, were found to be correlated with dust features visible in the f220 map. Large scale dust features, mostly at low Galactic latitude, can be seen in Figure 5. Objects that are located in dusty regions are indicated with a non-zero value for `dustFlag` in the cluster catalog (see Table A3).
3. *Extended objects.* Objects in the local Universe with large angular size, such as nearby galaxies and planetary nebulae, can also cause spurious detections in the filtered maps. We therefore flag circular regions, of radius 1.2 times the total elliptical aperture radius, around objects listed in the 2 Micron All Sky Survey (2MASS) Large Galaxy Atlas (Jarrett et al. 2003). We also flag circular regions around all objects with radius $> 1'$ in the New General Catalog (NGC2000 version; Sinnott 1988). Objects located within regions containing extended foreground objects are indicated with a non-zero value for `extObjFlag` in the cluster catalog (see Table A3).

4. *Bright stars.* It is difficult to optically confirm and measure photometric redshifts for cluster candidates that are near bright stars. We use *W1*-band ($3.4\ \mu\text{m}$ wavelength) magnitude measurements in the AllWISE catalog (produced by the Wide-field Infrared Survey Explorer (WISE) mission; Wright et al. 2010; Mainzer et al. 2011) to identify such regions. We mask circular regions of radius $3.5'$ ($3 < W1 < 7\ \text{mag}$); $7'$ ($-1 < W1 < 3\ \text{mag}$); and $10'$ ($W1 < -1\ \text{mag}$). Objects located close to bright stars are indicated with a non-zero value for `starFlag` in the cluster catalog (see Table A3).

There are also two, separate flag classes that are not recorded in the flag mask:

1. *Ring artifacts around high S/N clusters.* Clusters with large SZ signals (e.g., El Gordo, Menanteau et al. 2012, detected at $S/N = 82$ in DR6) can induce ringing artifacts in the filtered maps, some of which have S/N above the object detection threshold. We identify candidate spurious ring features by creating a segmentation map that identifies objects made from a minimum of 30 connected pixels with $S/N > 0.5$. When constructing the cluster catalog, we then check if an object is found in this candidate ring mask. If the object is then found to be located within $12'$ of another cluster candidate detected with $S/N > 20$, the object is flagged as a ring artifact (`ringFlag` = 1 in the cluster candidate list). For convenience, we increment the `flags` value of the object in the cluster catalog as well.
2. *Objects split across tile boundaries.* Some high S/N cluster candidates detected at the edge of a tile may be detected in more than one tile. Objects which are located within $2.5'$ of another candidate found in a different tile have the `tileBoundarySplit` flag set in the cluster candidate list produced by NEMO. These are then visually inspected in the filtered maps, and the candidate corresponding to the part of the cluster that ‘leaked’ across the tile boundary (generally the candidate with the lower S/N , corresponding to the edge rather than center of a cluster) is rejected when the final cluster catalog is assembled. This process could be automated or avoided entirely with some modifications to NEMO, but this is left to future work as this situation occurs rarely in the ACT DR6 catalog (only 47 out of 21558 candidates have `tileBoundarySplit` = 1).

Pixels (and in turn cluster candidates) may be flagged multiple times using the above criteria. The `flags` value in the catalog contains the sum across all the above categories, except for `tileBoundarySplit` (see Table A3). Hence, a conservative, clean catalog can be selected by choosing only objects for which `flags` = 0. This corresponds to 15752 out of 21558 candidates detected with $\tilde{q} > 4$. We focus on this subsample of objects for the results presented in this work, but the full list of candidates, regardless of `flags` level, is included in the data products released with this paper.

2.3. False Positive Rate

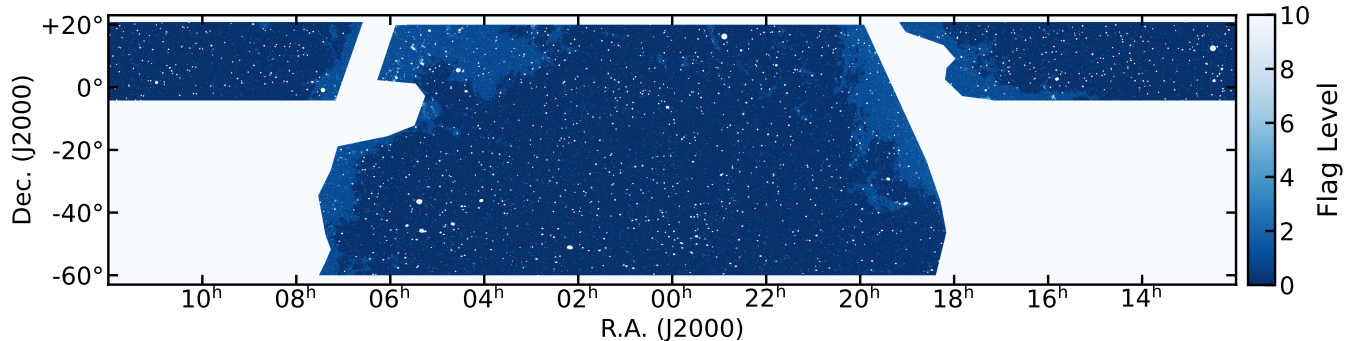


Figure 5. Flag values across the cluster search region, used to identify objects located in potentially problematic regions (see Section 2.2.3). Regions where `flags = 0` are taken to be ‘clean’; most of the `flags = 1` region corresponds to the dust mask; and regions with larger flag values contain point sources (e.g. AGNs and dusty galaxies) detected by ACT. The full 16293 deg^2 cluster search area (before masking and flagging) is shown as the black outline. The total ‘clean’ area within this covers 12590 deg^2 .

We estimate the expected number of false positive detections in the cluster candidate list by running NEMO on signal-free simulations, using a similar method to that described in Section 2.2.2 above. We create simulated `f090`, `f150`, and `f220` maps that contain CMB, $1/f$ noise, and white noise that follows the inverse variance maps produced by the map maker (Naess et al. 2025). We scale the white noise level up by a factor of 1.16 across all the simulated frequency maps, which results in the output noise map estimated by NEMO having the same median level (to within 2%) of the noise map obtained from running on the real data.⁶ We do this because the simulations do not contain point sources, or other astrophysical components (e.g., dust, Cosmic Infrared Background), resulting in an underestimate of the noise level seen in the real data. As the simulations do not contain point sources, we only run Steps 3–4 of the detection algorithm described in Section 2.2.2. Nevertheless, this exercise gives an idea of the expected false positive cluster candidate detection rate due to noise fluctuations, and is consistent with the fraction of optically confirmed clusters detected as a function of S/N in the real data, as shown in Section 3.2.

Figure 6 shows the results for the `flags = 0` area within the Legacy footprint, which are similar to those reported in H21 for this exercise. This shows that we expect only 11 false detections due to noise fluctuations in the Legacy footprint for the $\tilde{q} > 5.5$ cut used to define the ‘Legacy sample’. This is a lower limit as the simulations used do not include all possible sources of contamination (e.g., artifacts related to point sources, dust, etc.).

2.4. Position Recovery

As in H21, we use source injection simulations to assess the accuracy of position recovery for cluster candidates. Note that this only accounts for the effect of noise fluctuations in the map, and not any other astrophysical causes (e.g., cluster mergers). We paint UPP model clusters into the real ACT frequency maps with uniformly distributed amplitudes and sizes selected from $\theta_{500c} (') \in \{7.8, 4.2, 2.4, 1.5\}$. We recover a total of $\approx 10^5$

⁶ Rescaling the white noise level has no effect on the number of false positive detections as a function of S/N \tilde{q} (i.e., this makes no difference to the results shown in Figure 6). We apply this factor only for consistency with the end-to-end simulations described in Appendix B.

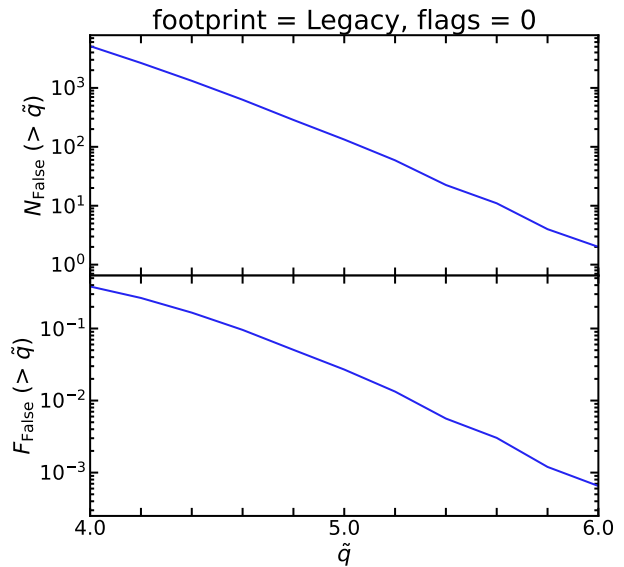


Figure 6. An estimate of the false positive cluster candidate detection rate in the `flags = 0` area of the 10317 deg^2 Legacy footprint. The top panel shows the cumulative number of detections as a function of signal-to-noise \tilde{q} in signal-free simulations (averaged over 10 realizations). The bottom panel presents the expected false positive fraction of the real cluster candidate list as a function of \tilde{q} cut.

detections with $\tilde{q} > 4$ over these injection runs. To quantify the accuracy of position recovery, we use the Rayleigh distribution,

$$P(\theta, \sigma) = \frac{\theta}{\sigma^2} \exp(-\theta^2/2\sigma^2), \quad (3)$$

where θ is the angle between the true and recovered cluster position, and σ is the scale parameter for the distribution.

Figure 7 shows the result of fitting Equation (3) to recovered position offsets, binned by \tilde{q} , to find σ . We find that a good fit to σ as a function of \tilde{q} is given by $\sigma = 1.428/\tilde{q}$, with σ specified in arcminutes. We make use of this model in cross-matching ACT cluster candidates against other cluster catalogs in Section 3.1 below.

2.5. Mass Estimates

We estimate cluster masses with the same methodology used for previous ACT cluster catalogs. The motivation for the method is described in H13. We assume that the

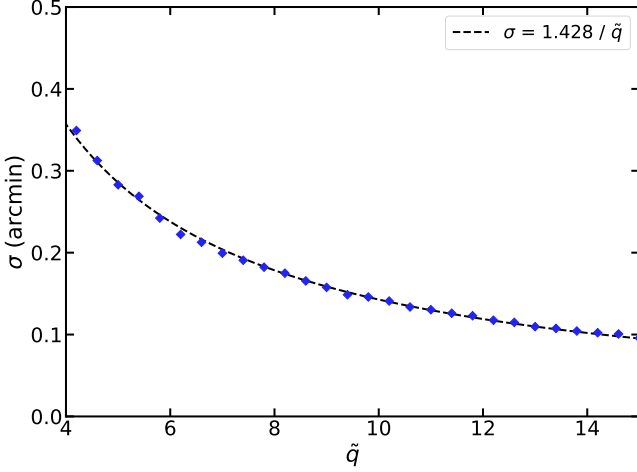


Figure 7. Results of fitting the distribution of recovered cluster position offsets obtained from source injection simulations with the Rayleigh distribution (Equation 3), as a function of signal-to-noise \tilde{q} . A single parameter model is a good description for how σ changes with \tilde{q} .

cluster central Comptonization parameter \tilde{y}_0 is related to mass via

$$\tilde{y}_0 = 10^{A_0} E(z)^2 \left(\frac{M_{500c}}{M_{\text{pivot}}} \right)^{1+B_0} Q(\theta_{500c}) f_{\text{rel}}(M_{500c}, z), \quad (4)$$

where 10^{A_0} is a normalization that sets the overall mass scale, $B_0 = 0.08$, $M_{\text{pivot}} = 3 \times 10^{14} M_{\odot}$, $Q(\theta_{500c})$ is the filter mismatch function (this accounts for the angular size difference between clusters with different masses and redshifts to the reference $2.4'$ filter scale used for measuring \tilde{y}_0 , see H13), and f_{rel} is a relativistic correction (implemented as described in H21, using the formulae of Itoh et al. 1998). $E(z)$ describes the evolution of the Hubble parameter in units of H_0 with redshift, i.e., $E(z) = (\Omega_m(1+z)^3 + \Omega_\Lambda)^{1/2}$.

In a departure from previous ACT cluster catalog papers, we adopt $10^{A_0} = 3.0 \times 10^{-5}$ as the normalization for the scaling relation, rather than the value derived from Arnaud et al. (2010, based on X-ray observations of low redshift clusters; $10^{A_0} = 4.95 \times 10^{-5}$, see H13), that was used for both previous ACT and *Planck* cluster catalogs. All figures in this paper that use the symbol M_{500c} assume $10^{A_0} = 3.0 \times 10^{-5}$. For comparison with previous work, we still report mass estimates that use the Arnaud et al. (2010) mass calibration in the cluster catalog (see Section 4), for which we use the symbol M_{500c}^{A10} . The $10^{A_0} = 3.0 \times 10^{-5}$ normalization chosen here, which is $\approx 60\%$ of the previous value, gives masses that are consistent with stacked weak-lensing analyses of the ACT DR5 cluster sample, for which $M_{500c}^{A10}/M_{500c}^{\text{WL}} = 1 - b = 0.65 \pm 0.05$ (Robertson et al. 2024, based on Kilo-Degree Survey [KiDS] data; which is consistent with results found by Shirasaki et al. 2024 using Hyper Suprime-Cam [HSC] data), where the superscript WL indicates the average stacked weak-lensing mass.

To obtain mass estimates from the SZ signal using Equation (4), correcting for the Eddington bias (Eddington 1913) due to the steepness of the halo mass function (HMF) and $\sigma_{\text{int}} = 0.2$ log normal intrinsic scatter (based on the results of numerical simulations, see H13), we use

the same method as in previous ACT cluster papers. We compute the posterior probability

$$P(M_{500c}|\tilde{y}_0, z) \propto P(\tilde{y}_0|M_{500c}, z)P(M_{500c}|z), \quad (5)$$

where $P(M_{500c}|z)$ is the HMF at redshift z , for which we use the implementation of the Tinker et al. (2008) HMF in the Core Cosmology Library v3.1.2 (CCL;⁷ Chisari et al. 2019). We assume $\sigma_8 = 0.80$ for HMF calculations throughout this work. The uncertainties we quote on our mass estimates account for measurement errors and the effect of intrinsic scatter, but otherwise do not include uncertainties on the scaling relation parameters themselves. We also provide a set of mass estimates in the cluster catalog (see Section 4) that do not include the Eddington bias correction, allowing them to be compared against, e.g., the mass estimates in the PSZ2 catalog (Planck Collaboration et al. 2016b).

2.6. Completeness

We estimate the completeness of the cluster sample as a function of mass by using a semi-analytic method that has been validated using end-to-end simulations, accounting for the optimization bias introduced by the matched filter (see Appendix B below). The overall approach is similar to that used by Planck Collaboration et al. (2016a). This accounts for the completeness due to the noise properties of the map, but does not account for the impact of sources correlated with clusters (see Section 5.2 below for a brief discussion of this issue).

We calculate the area-weighted average completeness χ above a given signal-to-noise cut \tilde{q}_{cut} on the (M_{500c}, z) grid over i patches in the map (with i different noise levels) using

$$\chi = \int d\ln\tilde{y}_0 P(\tilde{y}_0|M_{500c}, z) \sum_i \chi_i(\tilde{q}) W_i, \quad (6)$$

where

$$P(\tilde{y}_0|M_{500c}, z) = \frac{1}{\sqrt{2\pi}\sigma_{\text{int}}} \exp \left[- \left(\frac{\ln\tilde{y}_0 - \ln\tilde{y}_0^{\text{corr}}}{\sqrt{2}\sigma_{\text{int}}} \right)^2 \right], \quad (7)$$

and

$$\chi_i(\tilde{q}) = \frac{1}{2} \left[1 - \text{erf} \left(\frac{\tilde{q}_{\text{cut}} - \tilde{q}_i}{\sqrt{2}} \right) \right]. \quad (8)$$

Here, \tilde{y}_0 is taken to be the true value obtained through Equation (4), neglecting the relativistic correction (as this is not significant for clusters near our chosen signal-to-noise cut), and $\tilde{y}_0^{\text{corr}}$ is this value with optimization bias applied, using the model described in Appendix B. The area weight for patch i is represented by W_i , and $\tilde{q}_i = \tilde{y}_0/\delta\tilde{y}_{0i}$, where $\delta\tilde{y}_{0i}$ is the noise level in patch i .

Figure 8 shows the area-weighted average completeness in the (M_{500c}, z) plane for $\tilde{q} > 5$ over the 12590 deg^2 flags = 0 search area, as calculated using Equation (6), assuming the scaling relation described by Equation (4), the optimization bias model described in Appendix B, log-normal intrinsic scatter, and Gaussian noise. At $z = 0.5$, the 90% mass completeness limit is $M_{500c} > 5.3 \times 10^{14} M_{\odot}$. For the Legacy footprint, the limit is

⁷ <https://github.com/LSSTDESC/CCL>

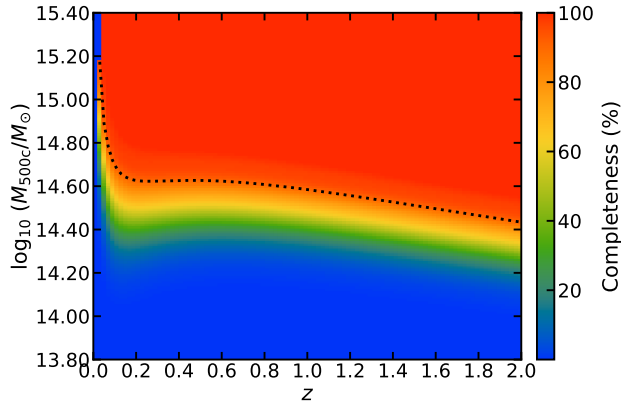


Figure 8. Completeness in the (M_{500c}, z) plane for a signal-to-noise cut $\tilde{q}_{\text{cut}} = 5$, for the `flags = 0` search area, calculated as described in Section 2.6. The dotted black line indicates the 90% completeness limit.

slightly lower, $M_{500c} > 5.0 \times 10^{14} M_{\odot}$. The mass limits within the DES, HSC, and KiDS footprints are similar. These mass limits are higher than those quoted in H21 due to the lower value of 10^{A_0} used in this work. The equivalent mass limit using the Arnaud et al. (2010) mass calibration is $M_{500c}^{A_{10}} > 3.0 \times 10^{14} M_{\odot}$ for DR6, compared to $M_{500c}^{A_{10}} > 3.8 \times 10^{14} M_{\odot}$ for DR5, as reported in H21.

The mass limit varies spatially, driven by the evolution of the ACT observing strategy from 2008 to 2022, as shown by the map in Figure 9. We plot the cumulative area as function of mass limit derived from this map in Figure 10. The deepest 20% of the full search area, covering 3237 deg^2 , is sensitive to clusters with lower limits to the mass lying in the range $2.9 < M_{500c}/10^{14} M_{\odot} < 3.5$.

3. OPTICAL/IR FOLLOW-UP AND REDSHIFTS

In this Section we describe the process of assigning redshifts to ACT cluster candidates, using the heterogeneous optical/IR data currently available over the large ACT cluster search area. The overall procedure is similar to that used in H21; here we aim to highlight differences with respect to the previous analysis, which come primarily from new redshift sources that were not available at the time of the ACT DR5 release. We may update the catalog of confirmed clusters with redshifts and mass estimates after publication as newer optical/IR data become available. If so, a set of DR6 cluster search data products with a new version number will be posted on LAMBDA.

3.1. Redshift Assignment

We assign redshifts to most of the cluster candidates through automated cross-matching against a set of cluster catalogs that we deem to be reliable, using a method that is more conservative than used in H21. In the previous analysis, we matched clusters using a combination of the ACT positional uncertainty, with an additional 0.5 Mpc projected distance cross-matching radius that was intended to account for ‘astrophysical’ uncertainties; i.e., miscentering in optical/IR catalogs (e.g., Zhang et al. 2019; Ding et al. 2025). While cross-matching using a large projected radius will result in a more complete sample, it carries the risk of matching low-richness clusters

in optical catalogs with noise fluctuations in the ACT map (see Section 2.3). Three such cases were identified by Ding et al. (2025) using the combination of ACT DR5 and HSC data.

We start by considering the Rayleigh distribution model fit shown in Figure 7. A fixed value of $\sigma = 0.357'$ corresponds to $\tilde{q} = 4$, which is the minimum S/N that we consider in our sample. The 99.7 percentile of this Rayleigh distribution corresponds to a cross-match distance of $1.22'$, which is equivalent to cross-matching within a projected distance between 0.24–0.61 Mpc over the redshift range $0.2 < z < 2$. For comparison, 95% of cluster centers are found within a 0.5 Mpc projected cross-match distance according to the Ding et al. (2025) model (which includes a miscentered component, and has been cleaned of non-astrophysical sources of miscentering), while 99.7% are found within 1 Mpc. We therefore choose to cross-match using the projected distance corresponding to $1.22'$ at the cluster redshift, if this is larger than 0.5 Mpc (where the ACT positional accuracy may be the dominant cause of miscentering), or otherwise use a projected cross-match radius of 0.5 Mpc. This choice is a compromise; it may result in up to 5% of clusters being missed by automated cross-matching, but it avoids the possibility of adding a number of spurious cross-matches (particularly at low redshift) that would result from using a 1 Mpc cross-match radius.

We perform automated cross-matching against cluster catalogs produced by the following teams: CAMIRA (Oguri 2014; Oguri et al. 2018, here we use the CAMIRA23B catalog; see Oguri et al., in prep.); eRASS1 (Bulbul et al. 2024); MaDCoWS (Gonzalez et al. 2019; Thongkham et al. 2024a,b); MCMF (Klein et al. 2023, 2024a); redMaPPer (Rykoff et al. 2014, 2016, here we use the v0.8.5 DES Y6 catalog); SPIDERS (Clerc et al. 2020; Kirkpatrick et al. 2021); SPT (Bleem et al. 2015, 2020, 2024); WaZP (Aguena et al. 2021; Benoist et al. 2025, here we use the v5.0.12.6801 DES Y6 catalog); and Wen & Han (2015).

Table 1 lists the total number of ACT DR6 cluster candidates cross-matched against cluster catalogs drawn from the DES and HSC surveys, and the chance association probability estimated from matching against ACT DR6 random catalogs. We choose to only consider the DES and HSC cluster catalogs here because estimating the chance association probability requires accurate knowledge of the area of intersection between the ACT cluster search area and the respective optical survey (this is not readily available in a convenient format for all the optical cluster catalogs that we cross-match against). We find that there is a 1-6% probability of matching an ACT DR6 cluster candidate against a cluster in these optical cluster catalogs by chance. For comparison, the less conservative automated cross-matching procedure used in constructing the ACT DR5 cluster catalog resulted in a 5% chance of ACT DR5 cluster candidates being randomly associated with redMaPPer or CAMIRA clusters (see H21). The chance association probability depends upon the details of how the optical cluster catalog was constructed and the cuts applied to the catalog.

We also estimate photo- z s using the zCLUSTER⁸ package, as described in H21, the only change being that

⁸ v0.5.1; <https://github.com/ACTCollaboration/zCluster>

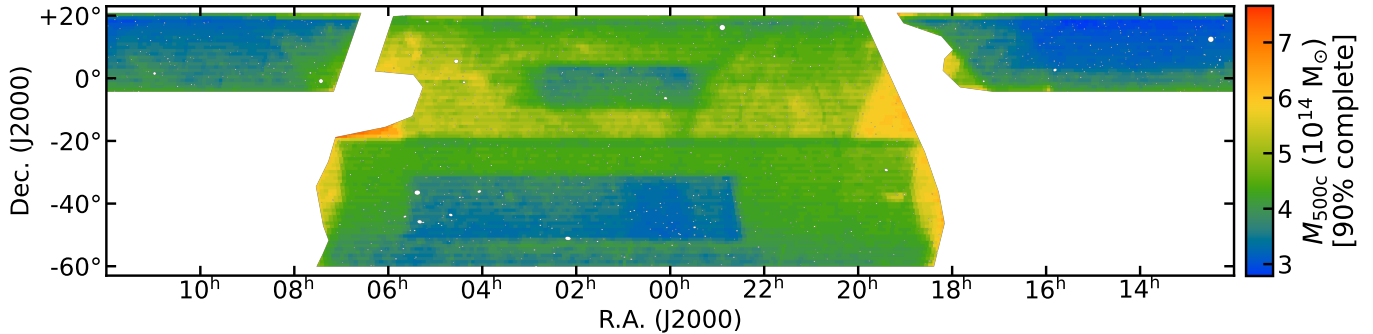


Figure 9. Mass limit map (90% completeness) for clusters with $\tilde{q}_{\text{cut}} = 5$, evaluated at $z = 0.5$ as described in Section 2.6. The spatial variation in the mass limit is largely a reflection of the ACT survey strategy, which evolved over the lifetime of the project.

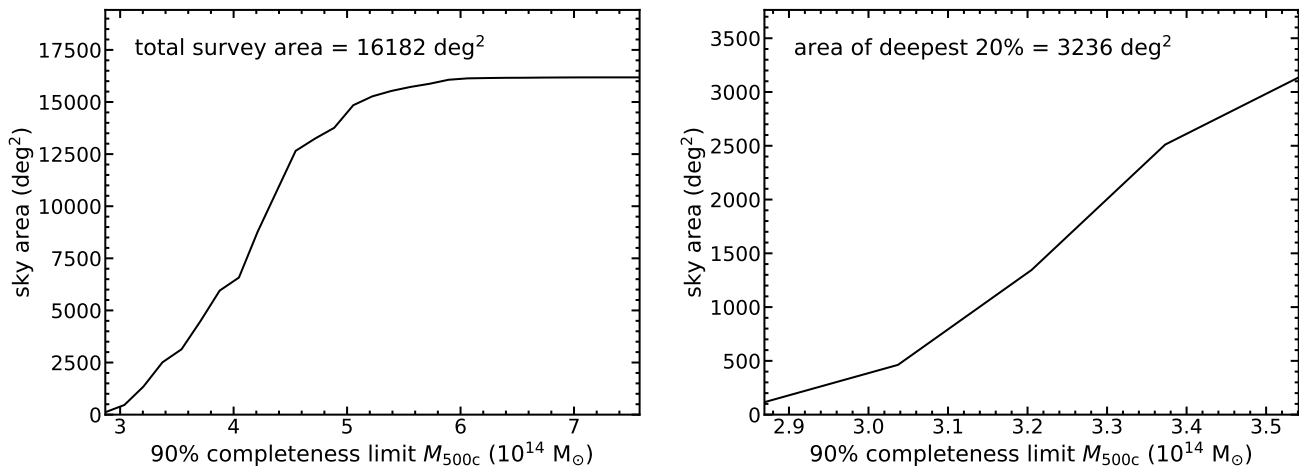


Figure 10. Sky area for which the signal-to-noise $\tilde{q} = 5$ cluster sample is at least 90% complete above the given mass limit for clusters with $z = 0.5$ (see Figure 8 for an illustration of the mild z -dependence over most of the redshift range). The left panel shows this for the full survey area, while the right panel shows this for the deepest 20% of survey area.

Table 1

Summary of the results of automated cross matching against DES and HSC optical cluster catalogs that intersect with the ACT cluster search area (see Section 3.1).

Catalog	Optical Survey	Cut Applied	Number of Matches	Chance Association Probability (%)
redMaPPer	DES Y6	$\lambda > 20$	2154	1.0
WaZP	DES Y6	WaZP SNR > 4	3204	6.4
CAMIRA	HSC Wide S23B	$N_{\text{mem}} > 16$	753	1.7

Note. — The Cut Applied column refers to a constraint placed on the input optical cluster catalog, which is either in terms of S/N reported in that catalog (WaZP), or richness (λ or N_{mem}).

here we use updated photometry from DR10.1 of the DESI Legacy Imaging Surveys (Dey et al. 2019). We ran zCLUSTER on all `flags = 0` candidates, and all $\tilde{q} > 5$ candidates with any `flags` value. We visually inspect the available optical/IR imaging before assigning a zCLUSTER redshift estimate to a candidate. As in H21, in the `warnings` field of the DR6 cluster catalog we indicate objects where the zCLUSTER optical density contrast statistic has a low value ($\delta < 3$), although this does not necessarily indicate that the redshift is unreliable.

After the above procedures were completed, we visually inspected WISE images of $\tilde{q} > 5.5$ candidates for which no redshift estimate was available. For those deemed to be high-redshift clusters, we estimated their redshifts by using an empirical relationship between the $W1 -$

$W2$ color of the object identified as the brightest central galaxy (BCG),

$$W1 - W2 = (1.52 \pm 0.08) \left(\frac{z}{1.2} \right) - (0.96 \pm 0.07), \quad (9)$$

(see Figure 11). This was obtained from a weighted least squares fit to WISE colors of 52 $0.8 < z < 1.6$ BCGs in clusters with spectroscopic redshifts taken from Stott et al. (2010); Lidman et al. (2013); Fassbender et al. (2011a,b); Santos et al. (2011), in addition to clusters with spectroscopic redshifts and BCG positions recorded in the ACT cluster catalog. Redshifts were assigned to 59 clusters using this procedure, by inverting Equation (9), with redshift uncertainty $\Delta z \approx 0.1$ resulting from the uncertainty in the fit parameters.

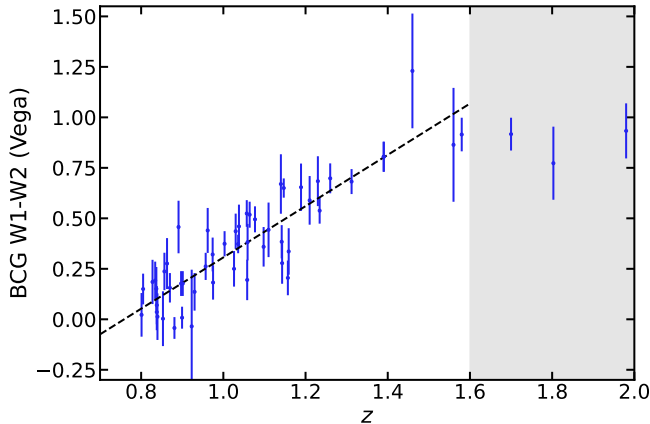


Figure 11. Relationship between WISE $W1 - W2$ color and z , derived from BCGs in clusters with spectroscopic redshifts (see Section 3.1). This arises because of the ‘stellar bump’ feature at $1.6\ \mu\text{m}$ in galaxy spectral energy distributions (e.g., Papovich 2008). The dashed line shows a weighted least squares fit to the data (Equation 9) over the range $0.8 < z < 1.6$. This was used to obtain redshift estimates for 59 clusters with no other redshift source available.

In addition to all of the above sources, we also used a number of redshifts from miscellaneous sources in the literature. Table 2 provides a full breakdown of all the redshift sources used in constructing the catalog.

The final catalog contains a single redshift estimate per candidate, using what we judged to be the best available redshift at the time of publication. We adopt spectroscopic redshifts where possible. Photometric redshifts assigned via automated cross-matching used the following order of preference: (1) redMaPPer in DES Y6; (2) CAMIRA S23B; (3) SPT; (4) MaDCoWS2 DR2; (5) WaZP in DES Y6; (6) eRASS1; (7) MCMF; (8) redMaPPer in SDSS; (9) Wen & Han (2015). To some extent this prioritizes cluster catalogs that used deeper optical data and/or incorporate WISE IR photometry.

Note that for many objects in the catalog where multiple photometric redshifts are available, the different redshift sources are usually consistent, so in practice the order of assignment for photo- z s does not have much impact on the resulting ACT DR6 cluster catalog (though it does impact the number of redshifts drawn from each source as listed in Table 2). However, we have identified 128 possible projected systems (i.e., candidates with plausible matches to multiple clusters along the line of sight), with many of these being identified after visual inspection of candidates with discrepant redshifts ($\Delta z > 0.5$) from multiple sources. These objects are indicated in the `warnings` field of the cluster catalog. Only one of these projected systems has so far been identified as a clearly blended detection in the SZ filtered map (ACT-CL J0335.1–4036, as first noted in H21).

Figure 12 shows optical/IR images of a selection of clusters drawn from the catalog, arranged by z and \tilde{q} .

3.2. Purity and Follow-up Completeness

As in previous ACT work (e.g., Menanteau et al. 2010, H21), we assess follow-up completeness from the fraction of cluster candidates with redshift estimates as a function of \tilde{q} cut. Figure 13 shows this for the `flags = 0` area in several footprints within the ACT cluster search area. We predict the purity of the sample as a function

of \tilde{q} cut using signal-free simulations (see Section 2.3) as $1 - F_{\text{False}}$, where F_{False} is the fraction of false positives, shown by the dashed line in Figure 13. This is expected to be the most optimistic case, as the signal-free simulations do not contain any source of contamination beyond that due to noise fluctuations in the map. Nevertheless, we see that the $1 - F_{\text{False}}$ line is a reasonable match to the fraction of detected, optically confirmed cluster candidates found in regions with deep optical data (DES, HSC; the small excess above the $1 - F_{\text{False}}$ line seen at $\tilde{q} \approx 4$ may result from spurious cross-matching of some optically selected clusters with SZ cluster candidates that are noise fluctuations). We find that the sample found within the $10317\ \text{deg}^2$ Legacy footprint is $> 99\%$ complete in terms of redshift follow-up for $\tilde{q} > 5.5$.

4. THE ACT DR6 CLUSTER CATALOG

4.1. Catalog Properties

The ACT DR6 cluster catalog consists of 10040 clusters detected at $\tilde{q} > 4$, with mass and redshift measurements. Of these, 8943 are located in the area with `flags = 0`. These are drawn from a full list of 21558 cluster candidates, though only 15752 of these have `flags = 0`. Table A3 gives descriptions of the columns in the cluster catalog.

We define a subset of 3747 clusters with $\tilde{q} > 5.5$ and `flags = 0` located within the $10317\ \text{deg}^2$ Legacy footprint⁹ as the ‘Legacy sample’, which we suggest for use in cosmological analyses that require a complete, statistical sample of clusters. Figure 14 shows the distribution of the cluster sample in terms of comoving distance in the celestial equatorial plane, with RA used as the angular coordinate. The ‘Legacy sample’, which is complete in terms of redshift follow-up, probes out to comoving distance ~ 5000 Mpc.

The mass and redshift distributions of the full cluster catalog are shown in Figure 15. The sample covers the mass range $1.3 < M_{500c}/10^{14}\ M_{\odot} < 22.9$, with median $M_{500c} = 2.8 \times 10^{14}\ M_{\odot}$. The sample covers the redshift range $0.03 < z < 2.00$, with median $z = 0.58$. It contains 4133 spectroscopic redshifts (41.2% of the sample). There are 1180 clusters at $z > 1$, of which 124 have redshifts estimated to be at $z > 1.5$. Many of these have photometric redshifts from the Klein et al. (2024a) and Thongkham et al. (2024b) catalogs, which used DESI Legacy Imaging Surveys data.

Figure 16 shows the ACT DR6 cluster sample in comparison to recent SPT surveys (Bleem et al. 2015, 2020, 2024; Klein et al. 2024b; Kornoelje et al. 2025), and the first release of the SRG/eROSITA cluster catalog in the Western Galactic hemisphere (eRASS1; Bulbul et al. 2024). All of these catalogs have approximately the same

⁹ The ‘Legacy’ footprint was defined from visual inspection of the confirmed cluster sample sky distribution, with reference to the dust mask. It is an attempt to define a region with the maximum contiguous area (split by the Galactic plane) that contains an almost complete sample of optically confirmed $\tilde{q} > 5.5$ clusters with redshifts (i.e., $> 99\%$ of $\tilde{q} > 5.5$ candidates within the ‘Legacy’ footprint are confirmed clusters). Note that the choice of the exact boundaries of this footprint are somewhat arbitrary. Users of the ACT DR6 cluster search data products can easily provide their own alternative mask to redefine this footprint if desired, see https://nemo-sz.readthedocs.io/en/latest/dr6_tutorial.html and <https://nemo-sz.readthedocs.io/en/latest/commands.html#nemomask>.

Table 2

Breakdown of redshift sources used in the ACT DR6 cluster catalog. The labels given in the Source column correspond to those used in the `redshiftSource` column in the FITS Table format cluster catalog (see Table A3).

Source	Number	Fraction (%)	Reference(s)
MaDCoWS	2575	25.6	Gonzalez et al. (2019); Thongkham et al. (2024a); Thongkham et al. (2024b)
redMaPPer	2019	20.1	Rykoff et al. (2014); Rykoff et al. (2016)
MCMF	1403	14.0	Klein et al. (2023); Klein et al. (2024b); Klein et al. (2024a)
PublicSpec	1223	12.2	Includes: 2dFLens, OzDES, SDSS, VIPERS, SPIDERS, DESI; Blake et al. (2016); Childress et al. (2017); Ahumada et al. (2020); Scodggio et al. (2018); Clerc et al. (2020); Kirkpatrick et al. (2021); DESI Collaboration (2025)
ACT	1049	10.4	Includes: zCLUSTER redshifts from this work; Menanteau et al. (2013b); Sifón et al. (2016); Hilton et al. (2018); Hilton et al. (2021)
WaZP	477	4.8	Aguena et al. (2021); Benoist et al. (2025)
SPT	436	4.3	Bocquet et al. (2019); Bleem et al. (2020); Bleem et al. (2024); Kor-noelje et al. (2025)
WH	295	2.9	Wen et al. (2012); Wen & Han (2015); Wen & Han (2022); Wen & Han (2024)
eRASS1	285	2.8	Bulbul et al. (2024)
CAMIRA	128	1.3	Oguri et al. (2018)
Lit	91	0.9	See table notes
WISEBCGz	59	0.6	This work
Total spectroscopic	4133	41.2	...
Total photometric	5907	58.8	...

Note. — Sources for literature redshifts: Struble & Rood (1991); Shectman et al. (1996); Smail et al. (1997); De Grandi et al. (1999); Struble & Rood (1999); Romer et al. (2000); Böhringer et al. (2000); Cruddace et al. (2002); Mullis et al. (2003); Valtchanov et al. (2004); Böhringer et al. (2004); Allen et al. (2004); Mullis et al. (2005); Burenin et al. (2007); Gilbank et al. (2008); Cavagnolo et al. (2008); Gal et al. (2009); Coziol et al. (2009); Gralla et al. (2011); Sanders et al. (2011); Chon & Böhringer (2012); Nastasi et al. (2014); Newman et al. (2014); Bradley et al. (2014); Stanford et al. (2014); Planck Collaboration et al. (2015); Pannuti et al. (2015); Planck Collaboration et al. (2016b); Adami et al. (2018); Willis et al. (2020); Ansarinejad et al. (2023)

mass calibration (to within $< 10\%$ on average). Both SPT-Deep and eRASS1 are sensitive to lower mass clusters than ACT DR6. The ACT DR6 catalog is the largest SZ-selected cluster catalog produced to date.

Inspection of Figure 16 shows that the most massive ACT DR6 clusters have higher inferred masses than objects in the eRASS1 catalog. Since ACT and eRASS1 have both surveyed a large fraction of the sky in common, this might suggest a shift in the inferred masses between the two catalogs. Figure 17 shows a comparison of the mass estimates reported for clusters in common between the two samples. We find that the average masses of the samples are consistent; $\langle M_{500c} [\text{eRASS1}] \rangle = (0.99 \pm 0.01) \langle M_{500c} \rangle$, where the uncertainty is the standard error on the mean. We note that the most massive clusters ($M_{500c} > 10^{15} M_{\odot}$) tend to have higher inferred masses in the ACT catalog. This could be due to physical reasons (e.g., mergers or line of sight projection effects, for example), but a detailed investigation is left for future work.

4.2. Other Cluster Search Data Products

We release a number of other data products related to the ACT DR6 cluster search:

1. *Candidate list.* The full list of 21558 $\tilde{q} > 4$ cluster candidates detected by NEMO. This includes objects detected in regions with high flag values, so this must be used with care.
2. *Multiple systems catalog.* We produce a catalog containing potential multiple systems, i.e., cluster

pairs, triples, etc. that may be physically associated, using the same method as described in H21 (we link objects located within a projected distance of 10 Mpc and within a line-of-sight velocity difference of 5000 km s^{-1}). One application of this kind of catalog is stacking to detect bridges between clusters, as done by Isopi et al. (2024). The largest multiple systems that we find contain four clusters, and there are three such systems which have spectroscopic redshifts for all components: ACT-CL J0857.8+0310 / J0857.9+0315 / J0859.5+0308 / J0901.5+0300 ($z = 0.20$); ACT-CL J0908.8+1102 / J0909.2+1058 / J0909.3+1104 / J0911.9+1057 ($z = 0.17$); and ACT-CL J1030.3+1403 / J1030.5+1415 / J1031.3+1405 / J1032.8+1352 ($z = 0.32$).

3. *Point source catalogs.* These are extracted from the f090, f150, and f220 maps as a byproduct of the NEMO cluster search (see Section 2.2.2), and are used in constructing the flag mask (see below). The catalogs included here include amplitude (ΔT), signal-to-noise, and position information. A dedicated search for point sources and a report on their properties will be presented in a future paper (Vargas et al., in prep.).
4. *Filtered maps.* Maps of \tilde{q} and \tilde{y}_0 ($\times 10^{-4}$) are provided in the standard ACT CAR pixelization as FITS images.
5. *Selection function information.* This includes masks (such as the flag mask; see Figure 5), noise

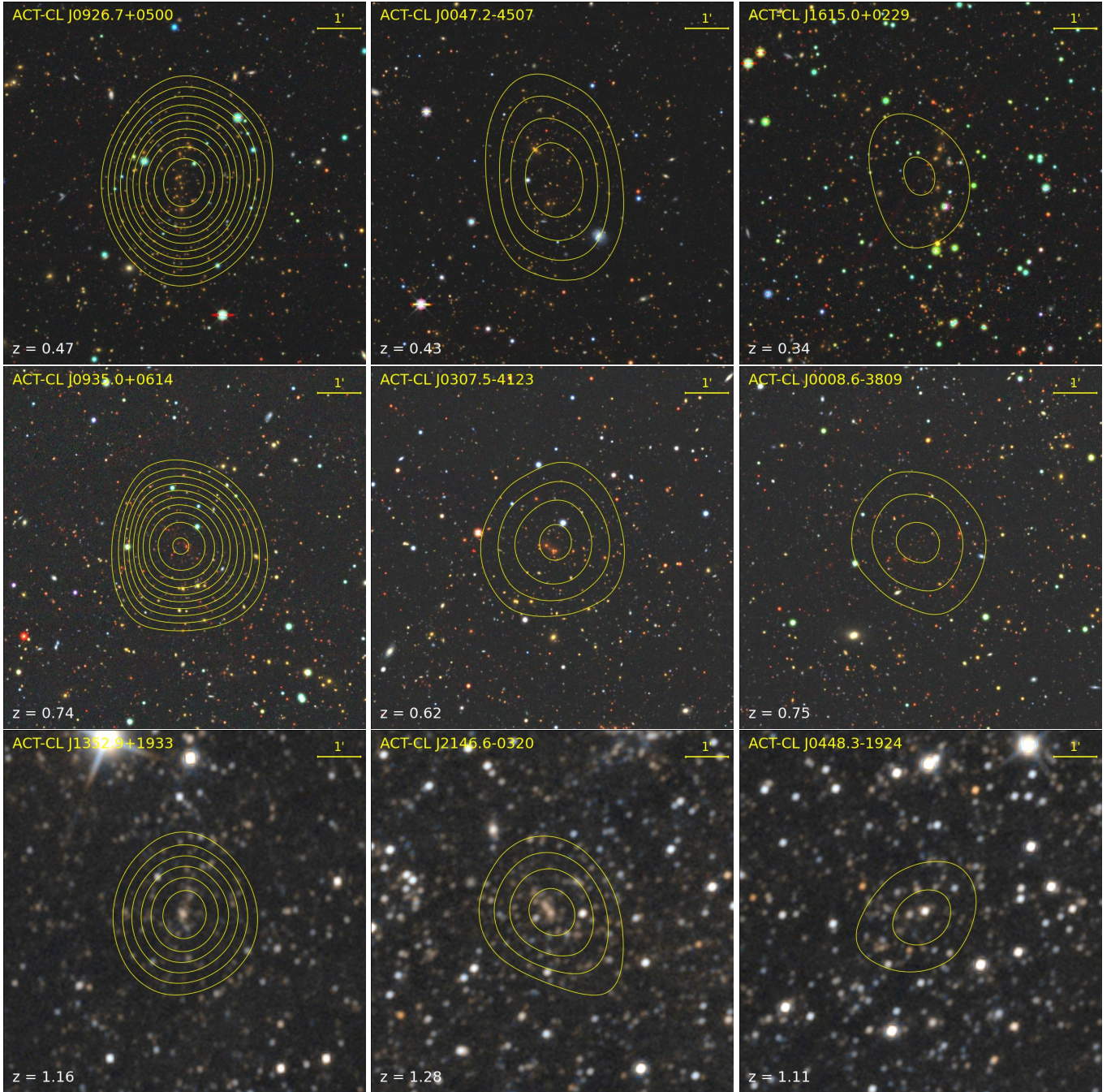


Figure 12. Example optical/IR images of clusters in the ACT DR6 catalog. Objects in columns from left to right have $\bar{q} > 20$, $10 < \bar{q} < 20$, and $5 < \bar{q} < 10$. Objects in rows from top to bottom have $0 < z < 0.5$, $0.5 < z < 1$, $1 < z < 1.5$. Images are taken from the DESI Legacy Imaging Surveys, with optical images (using g , r , z data) shown in the first two rows, and WISE IR images (using $W1$, $W2$ data) shown in the bottom row. The contours mark regions of constant signal-to-noise in the ACT filtered map, running from 3 – 25 σ , with a 2 σ interval between each contour.

tables and maps for various footprints that intersect with the ACT cluster search area (HSC, DES, KiDS, and the Legacy footprint), and tables that allow the filter mismatch function ($Q(\theta_{500c})$, see Section 2.5) to be computed.

6. *Cluster signal maps.* These are FITS images in the standard ACT CAR pixelization that allow the cluster thermal SZ signal to be subtracted from the f090, f150, and f220 maps. Note that the estimate of cluster size is quite noisy, and better results may

be obtained by using more filter scales than have been used for the ACT DR6 analysis. The UPP (Arnaud et al. 2010) is assumed. Tools are available in NEMO to make these model maps with different parameters.

Most of these data products can be reproduced by running NEMO on the public ACT DR6 maps.¹⁰

¹⁰ See https://nemo-sz.readthedocs.io/en/latest/dr6_tutorial.html

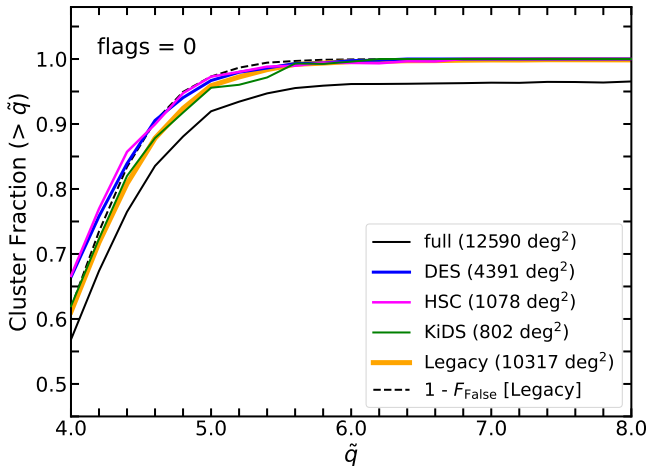


Figure 13. The fraction of DR6 cluster candidates with redshift measurements as a function of signal-to-noise \tilde{q} in $\text{flags} = 0$ areas of the cluster search region, within various different footprints (solid colored lines). The dashed line (labeled $1 - F_{\text{False}}$) shows the expected purity of the cluster sample within the Legacy footprint, based on signal-free simulations (see Section 2.3). Redshift follow-up is $> 99\%$ complete for $\tilde{q} > 5.5$ in the Legacy footprint. The full $\text{flags} = 0$ search area, which includes regions at low Galactic latitude, is $> 90\%$ complete in terms of redshift follow-up (i.e., 90% of candidates have been assigned redshifts) for $\tilde{q} > 5.0$. The slight excess above the $1 - F_{\text{False}}$ line at $\tilde{q} \approx 4$ in the DES and HSC regions is consistent within the expected shot noise, given the number of cluster candidates.

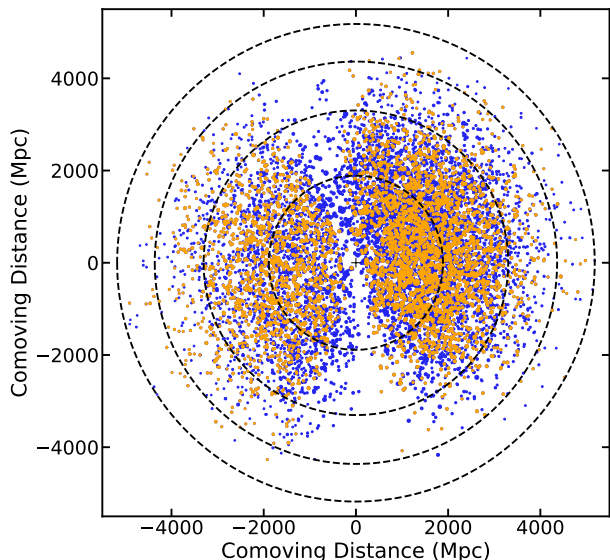


Figure 14. Wedge plot showing the full ACT DR6 cluster catalog (10040 blue points), and the ‘Legacy sample’ (3747 orange points), drawn in the equatorial plane. The size of each point scales with cluster mass. RA is used as the angular coordinate, with 0 deg RA pointing to the right from the origin and increasing counterclockwise. The radial coordinate is comoving distance in Mpc. The dashed circles mark the distances equivalent to redshifts 0.5, 1.0, 1.5, and 2.0, starting from the observer’s location at (0, 0).

5. DISCUSSION

5.1. Comparison with the ACT DR5 cluster catalog

We find that 508 clusters from the ACT DR5 catalog (H21) are not found in the DR6 catalog. Differences in masking account for 22 of these (i.e., 4173/4195 of the DR5 clusters are located within the DR6 cluster search

region, leaving 486 clusters from DR5 that are not found in the DR6 cluster catalog). The difference in the signal-to-noise selection criterion between the DR5 and DR6 analyses accounts for a further 126 objects; in DR6, we require $\tilde{q} > 4$ for inclusion in the catalog, whereas for DR5 we included all clusters detected with $S/N > 4$, regardless of the filter scale at which the object was detected. So, 360/4173 (8.6%) of clusters with $\tilde{q} > 4$ in the DR5 catalog that are within the DR6 cluster search area are missing in DR6.

All of the clusters previously reported in DR5 and missing from the DR6 catalog were optically confirmed. Most are also found in other catalogs, with 47% of the missing clusters coming from the redMaPPer catalogs that provided the most redshifts overall in DR5. They all have richness $\lambda > 20$, with median $\lambda = 40$ (for SDSS redMaPPer clusters) and $\lambda = 34$ (for DES redMaPPer clusters). These red sequence richnesses can be boosted by projection, and as a result the halo mass and SZ signal for these systems has a significant skew to low values (Cohn et al. 2007; DES Collaboration et al. 2025).

Another explanation for the disappearance of these clusters below our selection threshold is that they were boosted to higher \tilde{q} in the DR5 catalog by noise fluctuations. Using NEMO to perform forced photometry in the DR6 \tilde{q} maps at the locations given in the DR5 catalog, we find that 178/354 (49%) of the missing clusters have $\tilde{q} > 3$. The median difference in signal-to-noise between the catalogs for the missing clusters is $\Delta\tilde{q} = \tilde{q}_{\text{DR5}} - \tilde{q}_{\text{DR6}} = 1.5$.

Comparing the redshifts of clusters in common between the DR5 and DR6 catalogs, the reported values have changed by $\Delta z > 0.1$ for 150 clusters, and by $\Delta z > 0.5$ for 23 clusters. In the latter case, this is due to projected systems (see Section 3.1), where in DR5 we misidentified a lower redshift cluster along the line of sight to the SZ source in some cases. Better optical/IR data and new optical/IR cluster catalogs that were not available when H21 was published have helped to identify these issues.

5.2. Source Contamination and SZ Selection

Incompleteness due to sources, either active galactic nuclei (AGN) or dusty star forming galaxies, filling in the SZ decrement signal has long been a concern (Lin et al. 2009; Sayers et al. 2013; Dicker et al. 2021, 2024), although studies to date have not revealed it to be a significant issue (Gupta et al. 2017; Bleem et al. 2024). To test this for the ACT DR6 sample, using NEMO we perform forced photometry in the \tilde{q} and \tilde{y}_0 filtered maps at the locations of X-ray selected clusters from the eRASS1 catalog (Bulbul et al. 2024), since we do not expect X-ray selected clusters to be sensitive to this selection effect (although some X-ray clusters may have their luminosities boosted by contamination by X-ray AGNs). We extract \tilde{q} and \tilde{y}_0 values at the positions of eRASS1 clusters in the valid ACT DR6 search area, and compute mass estimates using Equation (4). Note that there are some eRASS1 clusters for which we adopt a different redshift estimate in the ACT DR6 catalog compared to that listed in the eRASS1 catalog; for estimating masses from forced photometry, we use the redshift as listed in the eRASS1 catalog. There are a total of 7043 eRASS1 clusters within the ACT footprint, and the forced photometry procedure returns 1690 of these with $\tilde{q} > 4$. It

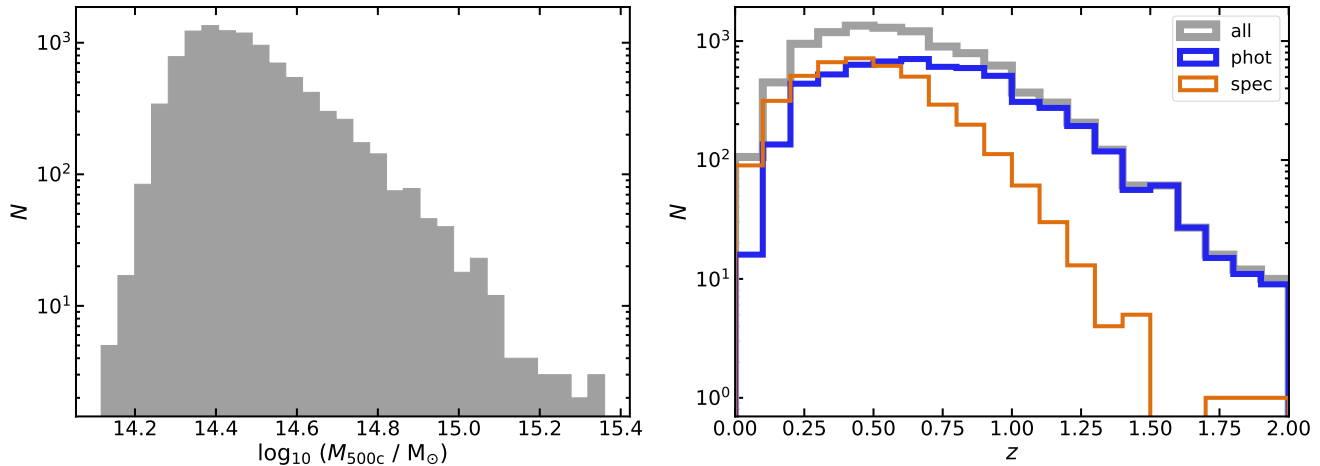


Figure 15. Mass and redshift distributions for the ACT DR6 cluster sample (see Section 4.1). In the right panel, objects with photometric redshifts are shown in blue, while those with spectroscopic redshifts (41.2% of the total sample) are shown in orange. The gray histogram shows the full sample.

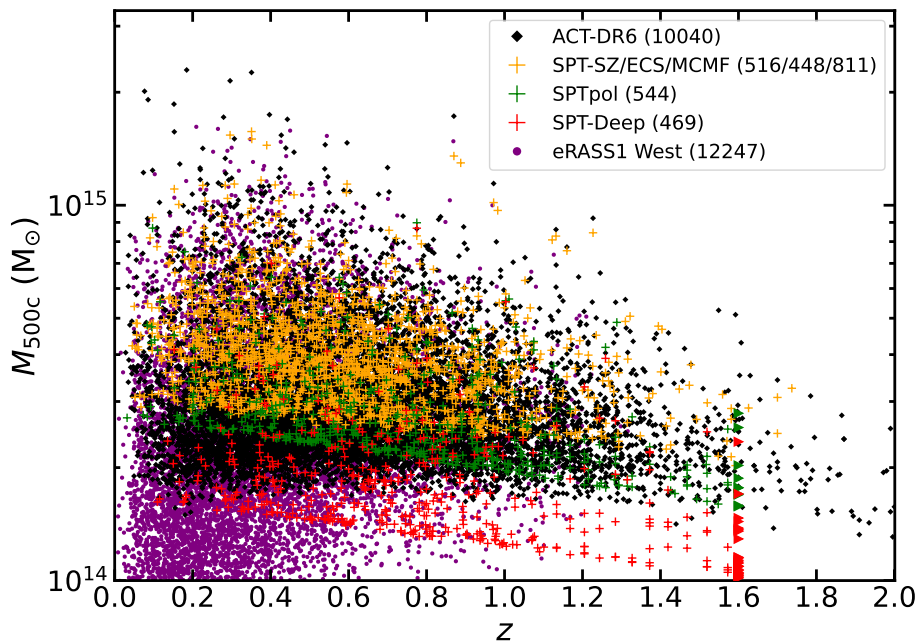


Figure 16. The ACT DR6 cluster sample in the (mass, redshift) plane, in comparison to recent SPT SZ cluster samples: SPT-SZ (Bleem et al. 2015); SPT-ECS (Bleem et al. 2020); SPT-MCMF (Klein et al. 2024b); SPTpol (Bleem et al. 2024); SPT-Deep (Kornelje et al. 2025); and the X-ray selected eRASS1 catalog in the Western Galactic hemisphere (Bulbul et al. 2024). Triangles indicate clusters with lower redshift limits in the SPTpol and SPT-Deep samples. The number of clusters in each sample is given in parentheses in the legend. All of these surveys are on comparable mass scales (to within $< 10\%$ on average).

is not surprising that most eRASS1 clusters are not detected by ACT, as most have masses below the ACT detection limit (see Figure 16). However, clusters that have large masses listed in the eRASS1 catalog that are missed by ACT can be used to investigate SZ incompleteness due to AGN contamination, under the assumption that the mass estimates provided by Bulbul et al. (2024) are reliable.

As shown in Section 2.6, the 90% mass completeness limit is approximately $M_{500c} > 5 \times 10^{14} M_{\odot}$ for $z > 0.2$ over most of the ACT cluster search area. There are 428 $z > 0.2$ eRASS1 clusters with eRASS mass estimates above this limit. Figure 18 shows a comparison between the SZ masses extracted via forced photometry, compared to the X-ray derived masses listed in the

eRASS1 catalog. We see overall agreement (most clusters scatter around the 1:1 line; see also Figure 17), but there is a tail of clusters with lower than expected SZ masses, given the eRASS1 mass.

We find $\tilde{q} > 5$ for 92% of the 428 clusters from the forced photometry procedure, while 32/428 clusters (7.5%) have $\tilde{q} < 5$. Of these, 14/33 have $3 < \tilde{q} < 5$. If we take the eRASS1 mass as ‘truth’, then this indicates there is suppression of the SZ signal in a small fraction of massive clusters. The most likely explanation for this would be contamination due to radio AGN (see also Dicker et al. 2021, 2024), though miscentring of the X-ray cluster position with respect to the peak of the SZ signal may also play a role (since forced photometry relies on the X-ray positions in the eRASS1 catalog).

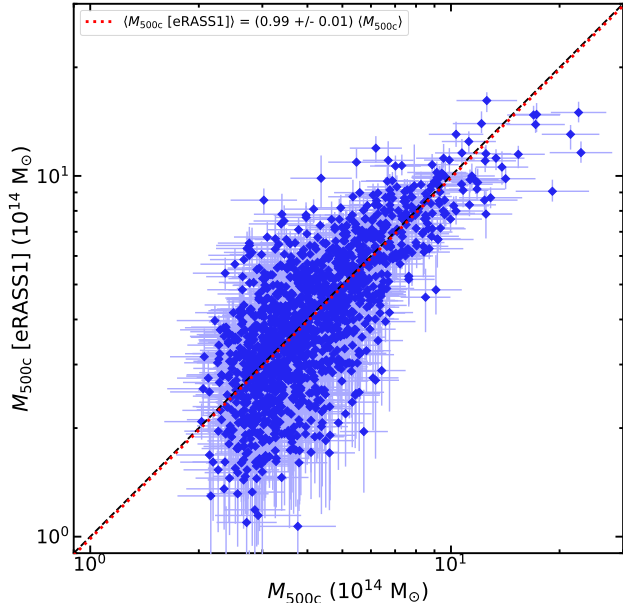


Figure 17. Comparison between ACT DR6 mass estimates (this work, plotted along the horizontal axis) and masses inferred from X-ray count rate measurements, calibrated using weak-lensing, as reported in the eRASS1 catalog (Bulbul et al. 2024; Ghirardini et al. 2024). The large blue points are objects with $\tilde{q} > 5$ in ACT DR6, for which the unweighted mean ratio between the two cluster samples is calculated, shown by the dotted red line. The dashed black line shows the 1:1 correlation.

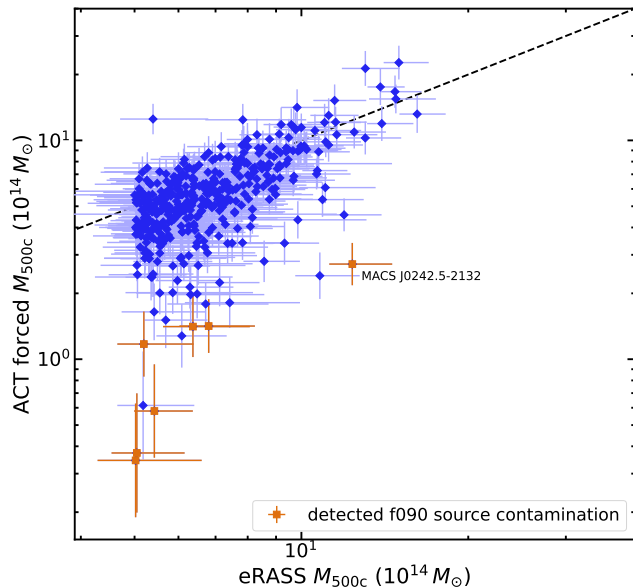


Figure 18. Comparison of SZ mass estimates extracted via forced photometry (vertical axis) with X-ray derived masses listed in the eRASS1 cluster catalog (horizontal axis), for clusters with eRASS $M_{500c} > 5 \times 10^{14} M_{\odot}$ and at $z > 0.2$ (approximately the $\tilde{q} > 5$ 90% mass completeness limit over the ACT DR6 search area). The dashed line shows the 1:1 relation, and demonstrates that the mass calibration used for both samples is comparable (see also Figure 17). Objects that were found to be located within $1.2'$ of a f090 point source are shown as the orange points. These have SZ mass estimates that are significantly lower than those measured by eROSITA. We highlight the case of MACS J0242.5-2132 (1eRASS J024235.9-213225), which is briefly discussed in Section 5.2.

In Figure 18, we highlight clusters which are found within $1.2'$ of a $S/N > 5$ f090 point source (there are a further four clusters which are not shown as they have negative \tilde{y}_0 values from the forced photometry). Note that sources are subtracted during the cluster detection procedure (see Section 2.2), so while this process has resulted in some SZ signal being recovered, it seems that this is not enough to match the mass inferred from the X-ray data. MACS J0242.5-2132 (Allen et al. 2004; also known as 1eRASS J024235.9-213225, with $M_{500c} > 10^{15} M_{\odot}$ at $z = 0.314$) is one example of a massive cluster that was missing in the ACT DR5 sample due to source contamination. This particular cluster hosts a compact radio source within the BCG with f090 flux density 65 mJy and 1.4 GHz flux density ≈ 1 Jy. It is recovered in the DR6 sample¹¹ at $\tilde{q} = 4.8$, and has an ACT mass estimate that is 22% of the eRASS1 mass estimate.

We found that 16/32 of the $\tilde{q} < 5$ clusters have positions that are offset from the SZ peak S/N location from visual inspection of the ACT filtered map, and so miscentring is most likely to be responsible for the lower than expected SZ signal for these systems. This includes one merging system that is visually resolved into two components by ACT, but which is not deblended in either the ACT or eRASS1 catalogs (ACT-CL J0810.3+1816 at $z = 0.42$, which is associated with 1eRASS J081025.1+181634). Miscentring can be due to radio sources affecting the SZ peak position, or positional uncertainties in the eRASS1 catalog.

We note that some eRASS1 clusters are blended in the ACT DR6 catalog, and are likely to be mergers. There are three such ACT detections that have multiple eRASS1 clusters within $< 1.2'$, which includes two mergers (both eRASS1 components at the same redshift; ACT-CL J0436.3-3317 at $z = 0.41$ and ACT-CL J0600.2-2007 at $z = 0.42$) and one possible projected system (ACT-CL J0547.1-5026, with eRASS1 clusters at $z = 0.68, 0.92$). Of these, only the eRASS1 clusters associated with ACT-CL J0600.2-2007 are part of the high-mass subsample with $M_{500c} > 5 \times 10^{14} M_{\odot}$, $z > 0.2$ considered above.

It is possible that some of the eRASS1 mass estimates may be biased high due to contamination by X-ray AGN, since X-ray count rate is the mass proxy used (see Bulbul et al. 2024; Ghirardini et al. 2024). Objects with potentially high X-ray AGN contamination are flagged using the PCONT quantity in the eRASS1 catalogs, which gives an estimate of the probability that the X-ray source is a contaminant rather than a cluster. We find that 4/33 of the $\tilde{q} < 5$ eRASS1 clusters have PCONT > 0.1 , and so their masses may be overestimated in the eRASS1 catalog.

After accounting for miscentring and X-ray AGN contamination, we conclude that radio source contamination directly results in 2–3% of $M_{500c} > 5 \times 10^{14} M_{\odot}$, $z > 0.2$ eRASS1 clusters being missed by ACT. The impact could be as high as 6%, if we include the miscentred clusters, assuming that they are affected by radio sources that are not directly detected by ACT. Obtaining a firmer estimate requires taking into account the details of the eRASS1 cluster selection and mass estimates. One

¹¹ Using NEMO v0.9.0; it was not recovered with $\tilde{q} > 4$ using earlier versions of the code.

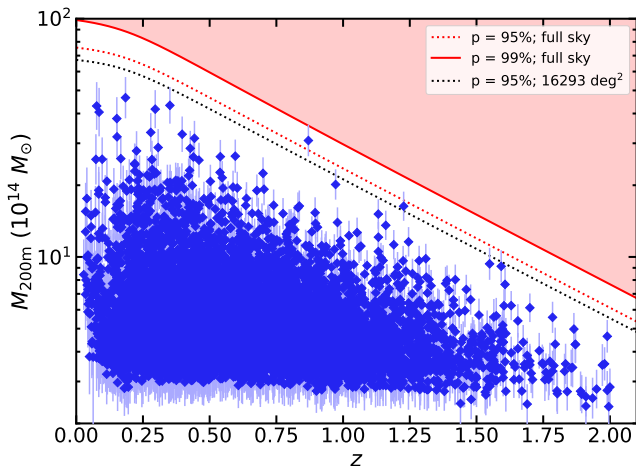


Figure 19. Mass and redshift distribution for the ACT DR6 catalog in terms of M_{200m} , compared to the flat Λ CDM exclusion curves of Mortonson et al. (2011), where the observation of even a single cluster above the shown lines conflicts with Λ CDM at the confidence level indicated in the figure legend. The two most extreme clusters are El Gordo at $z = 0.87$ (Menanteau et al. 2012), and ACT-CL J0329.2–2330 at $z = 1.23$ (Bleem et al. 2020; Sikhosana et al. 2025), which are both undergoing mergers that may have boosted their SZ-inferred mass estimates. (see Section 5.3).

should also note that the uncertainties on the SZ and X-ray signals considered here are at the $> 10\%$ level, and there may be other factors that cause the large intrinsic scatter seen in Figure 18. A more detailed investigation, perhaps involving higher resolution SZ observations (e.g., Dicker et al. 2021, 2024), would help to clarify this issue.

5.3. Extreme Clusters

Thanks to the large sky area covered by ACT and the redshift independent SZ effect, we have now searched for massive clusters in a large fraction of the universe out to $z = 2$. Here we revisit the question of whether any sufficiently massive clusters exist at early times in the universe that can rule out the Λ CDM cosmological model with Gaussian initial conditions, given the expected time needed for such massive structures to grow (e.g., Mortonson et al. 2011; Harrison & Coles 2012; Sahlén et al. 2016). We find that for the ACT DR6 catalog the answer is ‘no’, as shown by Figure 19. However, there are two clusters that lie over the 95% line as calculated for the ACT DR6 footprint. These are El Gordo (Menanteau et al. 2012), a spectacular merging system that remains the most extreme object in the ACT sample, despite the vastly increased sky area covered by ACT DR6 compared to ACT DR1, and ACT-CL J0329.2–2330 at $z = 1.23$ (first reported by SPT; Bleem et al. 2020). Like El Gordo, the latter system hosts a giant radio halo (Sikhosana et al. 2025), a turbulence-driven form of diffuse radio emission often seen in cluster mergers (see the review by van Weeren et al. 2019). Therefore it could be the case that the masses inferred for these systems from the SZ signal are overestimated, due to merger boosting as seen in hydrodynamical simulations (Poole et al. 2007; Wik et al. 2008; Krause et al. 2012). These simulations show that such merger boosting is expected to be transient, lasting for ~ 100 Myr. For El Gordo, the SZ-derived mass in ACT DR6 is $\approx 30\%$ higher than the weak-lensing mass measured by Kim et al. (2021), al-

though the two mass estimates only differ at the 1.4σ level. Adopting the Kim et al. (2021) weak-lensing mass for El Gordo would move it below the black dotted line ($p = 95\%$, 16293 deg^2) in Figure 19.

6. SUMMARY

This work presents the cluster catalogs and several of their properties derived from the ACT DR6 maps, using data obtained over the lifetime of the project (2008–2022). This includes a catalog of 10040 optically confirmed clusters with redshifts and mass estimates, covering the redshift range $0 < z < 2$ (median $z = 0.58$), with 1180 clusters at $z > 1$, largely made possible due to the overlap with recent optical/IR catalogs exploiting the DESI Legacy Imaging Surveys (Dey et al. 2019), including Thongkham et al. 2024a and Klein et al. 2024a. It is the largest SZ-selected cluster catalog to date, being a factor of > 2 larger than the ACT DR5 catalog (H21), and > 1.5 times larger than the ACT-DR5 MCMF catalog (Klein et al. 2024a).

Using an SZ-signal–mass scaling relation that is consistent with recent weak-lensing analyses (Robertson et al. 2024; Shirasaki et al. 2024), we find the confirmed clusters span the mass range $1.3 < M_{500c}/10^{14} M_{\odot} < 22.9$, with median $M_{500c} = 2.8 \times 10^{14} M_{\odot}$. We find that the 90% completeness limit at $\tilde{q} = 5$ is $M_{500c} = 5 \times 10^{14} M_{\odot}$ over most of the survey area. We find no evidence for a single cluster massive enough to falsify Λ CDM; El Gordo (Menanteau et al. 2012), discovered early in the history of the project, remains the most extreme cluster found by ACT, though we again note that the mass determined for El Gordo from weak lensing (Kim et al. 2021) is $\approx 30\%$ lower than the ACT SZ-derived estimate.

NEMO, the cluster and source detection package used to produce many of the results shown in this work, is publicly available under a free software license, and its documentation includes instructions on how to reproduce many of the ACT DR6 cluster search data products. It should also be capable of analyzing future maps from the Simons Observatory Large Aperture Telescope, which is expected to produce a catalog of $> 30,000$ galaxy clusters (Ade et al. 2019; The Simons Observatory Collaboration et al. 2025).

We thank the referee for some suggestions which helped to improve the quality of this paper.

Support for ACT was through the U.S. National Science Foundation through awards AST-0408698, AST-0965625, and AST-1440226 for the ACT project, as well as awards PHY-0355328, PHY-0855887 and PHY-1214379. Funding was also provided by Princeton University, the University of Pennsylvania, and a Canada Foundation for Innovation (CFI) award to UBC. ACT operated in the Parque Astronómico Atacama in northern Chile under the auspices of the Agencia Nacional de Investigación y Desarrollo (ANID). The development of multichroic detectors and lenses was supported by NASA grants NNX13AE56G and NNX14AB58G. Detector research at NIST was supported by the NIST Innovations in Measurement Science program. Computing for ACT was performed using the Princeton Research Computing resources at Princeton University and the Niagara supercomputer at the SciNet HPC Consortium. SciNet

is funded by the CFI under the auspices of Compute Canada, the Government of Ontario, the Ontario Research Fund–Research Excellence, and the University of Toronto. This research also used resources of the National Energy Research Scientific Computing Center (NERSC), a U.S. Department of Energy Office of Science User Facility located at Lawrence Berkeley National Laboratory, operated under Contract No. DE-AC02-05CH11231 using NERSC award HEP-ERCAPmp107 from 2021 to 2025. We thank the Republic of Chile for hosting ACT in the northern Atacama, and the local indigenous Licanantay communities whom we follow in observing and learning from the night sky.

We are grateful to the NASA LAMBDA archive for hosting our data. This work uses data from the Planck satellite, based on observations obtained with Planck (<http://www.esa.int/Planck>), an ESA science mission with instruments and contributions directly funded by ESA Member States, NASA, and Canada.

MH and KM acknowledge support from the National Research Foundation of South Africa (grant nos. 97792, 137975, CPRR240513218388). Computations were performed on Hippo at the University of KwaZulu-Natal, and at the Centre for High Performance Computing (project ASTR1534). This work was performed in part at the Aspen Center for Physics, which is supported by a grant from the Simons Foundation (1161654, Troyer). CS acknowledges support from the Agencia Nacional de Investigación y Desarrollo (ANID) through Basal project FB210003. MM acknowledges support from NSF grants AST-2307727 and AST-2153201 and NASA grant 21-ATP21-0145. JD acknowledges support from NSF grant AST-2108126, from a Royal Society Wolfson Visiting Fellowship and from the Kavli Institute for Cosmology Cambridge and the Institute of Astronomy, Cambridge. KMH is supported by NSF award 2206344. AN acknowledges support from the Horizon 2020 ERC Starting Grant (project number 101163128). ADH acknowledges support from the Sutton Family Chair in Science, Christianity and Cultures, from the Faculty of Arts and Science, University of Toronto, and from the Natural Sciences and Engineering Research Council of Canada (NSERC) [RGPIN-2023-05014, DGEGR-2023-00180].

The Legacy Surveys consist of three individual and complementary projects: the Dark Energy Camera Legacy Survey (DECaLS; Proposal ID #2014B-0404; PIs: David Schlegel and Arjun Dey), the Beijing-Arizona Sky Survey (BASS; NOAO Prop. ID #2015A-0801; PIs: Zhou Xu and Xiaohui Fan), and the Mayall z-band Legacy Survey (MzLS; Prop. ID #2016A-0453; PI: Arjun Dey). DECaLS, BASS and MzLS together include data obtained, respectively, at the Blanco telescope, Cerro Tololo Inter-American Observatory, NSF’s NOIRLab; the Bok telescope, Steward Observatory, University of Arizona; and the Mayall telescope, Kitt Peak National Observatory, NOIRLab. Pipeline processing and analyses of the data were supported by NOIRLab and the Lawrence Berkeley National Laboratory (LBNL). The Legacy Surveys project is honored to be permitted to conduct astronomical research on Iolkam Du’ag (Kitt Peak), a mountain with particular significance to the Tohono O’odham Nation.

NOIRLab is operated by the Association of Universities for Research in Astronomy (AURA) under a cooper-

ative agreement with the National Science Foundation. LBNL is managed by the Regents of the University of California under contract to the U.S. Department of Energy.

This project used data obtained with the Dark Energy Camera (DECam), which was constructed by the Dark Energy Survey (DES) collaboration. Funding for the DES Projects has been provided by the U.S. Department of Energy, the U.S. National Science Foundation, the Ministry of Science and Education of Spain, the Science and Technology Facilities Council of the United Kingdom, the Higher Education Funding Council for England, the National Center for Supercomputing Applications at the University of Illinois at Urbana-Champaign, the Kavli Institute of Cosmological Physics at the University of Chicago, Center for Cosmology and Astro-Particle Physics at the Ohio State University, the Mitchell Institute for Fundamental Physics and Astronomy at Texas A&M University, Financiadora de Estudos e Projetos, Fundação Carlos Chagas Filho de Amparo, Financiadora de Estudos e Projetos, Fundação Carlos Chagas Filho de Amparo à Pesquisa do Estado do Rio de Janeiro, Conselho Nacional de Desenvolvimento Científico e Tecnológico and the Ministerio da Ciencia, Tecnologia e Inovacao, the Deutsche Forschungsgemeinschaft and the Collaborating Institutions in the Dark Energy Survey. The Collaborating Institutions are Argonne National Laboratory, the University of California at Santa Cruz, the University of Cambridge, Centro de Investigaciones Energéticas, Medioambientales y Tecnológicas-Madrid, the University of Chicago, University College London, the DES-Brazil Consortium, the University of Edinburgh, the Eidgenössische Technische Hochschule (ETH) Zurich, Fermi National Accelerator Laboratory, the University of Illinois at Urbana-Champaign, the Institut de Ciències de l’Espai (IEEC/CSIC), the Institut de Física d’Altes Energies, Lawrence Berkeley National Laboratory, the Ludwig Maximilians Universität München and the associated Excellence Cluster Universe, the University of Michigan, NSF’s NOIRLab, the University of Nottingham, the Ohio State University, the University of Pennsylvania, the University of Portsmouth, SLAC National Accelerator Laboratory, Stanford University, the University of Sussex, and Texas A&M University.

The Legacy Survey team makes use of data products from the Near-Earth Object Wide-field Infrared Survey Explorer (NEOWISE), which is a project of the Jet Propulsion Laboratory/California Institute of Technology. NEOWISE is funded by the National Aeronautics and Space Administration.

The Legacy Surveys imaging of the DESI footprint is supported by the Director, Office of Science, Office of High Energy Physics of the U.S. Department of Energy under Contract No. DE-AC02-05CH1123, by the National Energy Research Scientific Computing Center, a DOE Office of Science User Facility under the same contract; and by the U.S. National Science Foundation, Division of Astronomical Sciences under Contract No. AST-0950945 to NOAO.

The Hyper Suprime-Cam (HSC) collaboration includes the astronomical communities of Japan and Taiwan, and Princeton University. The HSC instrumentation and software were developed by the National Astronomical

Observatory of Japan (NAOJ), the Kavli Institute for the Physics and Mathematics of the Universe (Kavli IPMU), the University of Tokyo, the High Energy Accelerator Research Organization (KEK), the Academia Sinica Institute for Astronomy and Astrophysics in Taiwan (ASIAA), and Princeton University. Funding was contributed by the FIRST program from the Japanese Cabinet Office, the Ministry of Education, Culture, Sports, Science and Technology (MEXT), the Japan Society for the Promotion of Science (JSPS), Japan Science and Technology Agency (JST), the Toray Science Foundation, NAOJ, Kavli IPMU, KEK, ASIAA, and Princeton University.

This paper makes use of software developed for Vera C. Rubin Observatory. We thank the Rubin Observatory for making their code available as free software at <http://pipelines.lsst.io/>.

This paper is based on data collected at the Subaru Telescope and retrieved from the HSC data archive sys-

tem, which is operated by the Subaru Telescope and Astronomy Data Center (ADC) at NAOJ. Data analysis was in part carried out with the cooperation of Center for Computational Astrophysics (CfCA), NAOJ. We are honored and grateful for the opportunity of observing the Universe from Maunakea, which has the cultural, historical and natural significance in Hawaii.

This research has made use of the NASA/IPAC Extragalactic Database, which is funded by the National Aeronautics and Space Administration and operated by the California Institute of Technology.

Software: AstroPy (Astropy Collaboration et al. 2013), Core Cosmology Library (Chisari et al. 2019), Pixell (<https://github.com/simonsobs/pixell/>)

APPENDIX

A. CONTENTS OF THE CLUSTER CATALOG

Table A3

Description of the columns in the FITS Table format cluster catalog, available from LAMBDA (https://lambda.gsfc.nasa.gov/product/act/actadv_dr6_szcluster_catalog_get.html). The Symbol column provides a mapping between column names and symbols used in the text and figures of this article.

Column	Symbol	Description
<code>name</code>	...	Cluster name in the format ACT-CL JHHMM.m±DDMM.
<code>RADeg</code>	...	Right Ascension in decimal degrees (J2000) of the SZ detection by ACT.
<code>decDeg</code>	...	Declination in decimal degrees (J2000) of the SZ detection by ACT.
<code>SNR</code>	q	Signal-to-noise ratio, optimized over all filter scales (in H21, the symbol SNR was used for this quantity).
<code>y_c</code>	y_0	Central Comptonization parameter ($\times 10^{-4}$) measured using the optimal matched filter template (i.e., the one that maximizes detection S/N q). Note that <code>inferred_y_c</code> provides a lower scatter estimate of this quantity. Uncertainty column(s): <code>err_y_c</code> .
<code>fixed_SNR</code>	\tilde{q}	Signal-to-noise ratio at the reference 2.4' filter scale (in H21, the symbol SNR _{2.4} was used for this quantity). This is the quantity used for estimating completeness.
<code>fixed_y_c</code>	\tilde{y}_0	Central Comptonization parameter ($\times 10^{-4}$) measured at the reference filter scale (2.4'). This is the SZ signal used for inferring mass estimates and estimating mass completeness limits (see Section 2.5). Uncertainty column(s): <code>fixed_err_y_c</code> .
<code>template</code>	...	Name of the matched filter template resulting in the highest S/N (q) detection of this cluster.
<code>tileName</code>	...	Name of the ACT map tile in which the cluster was found.
<code>flags</code>	...	Number of times a location on the sky was flagged, for whatever reason (see Section 2.2.3). Use <code>flags = 0</code> to select 'clean' regions. Note that many regions are flagged due to the presence of bright stars (which make obtaining photometric redshifts difficult or impossible), and the flagging set-up used for ACT DR6 is conservative.
<code>finderFlag</code>	...	Number of times a location on the sky was flagged during cluster finding. A non-zero value for this quantity indicates that a point source was subtracted at this location. As the point source subtraction process is not perfect, objects with this flag should be treated with care (see Section 2.2.3).
<code>starFlag</code>	...	If non-zero, indicates an area of sky close to a bright star. While this should not affect detection of the SZ signal, it may make it difficult or impossible to obtain a redshift estimate for this object (see Section 2.2.3).
<code>extObjFlag</code>	...	If non-zero, indicates an area of sky associated with an extended foreground object, such as a galaxy or a nebula (see Section 2.2.3).
<code>dustFlag</code>	...	If non-zero, indicates an area of sky that is dusty, as traced by emission in the <i>Planck</i> 353 GHz map (see Section 2.2.3).
<code>ringFlag</code>	...	If non-zero, indicates an object flagged as a possible ring artifact. It may be that the object is in fact a cluster. If so, the SZ signal may have been artificially boosted by the presence of the ring, so use these objects with care (see Section 2.2.3).
<code>redshift</code>	z	Adopted redshift for the cluster. The uncertainty is only given for photometric redshifts. Uncertainty column(s): <code>redshiftErr</code> .
<code>redshiftType</code>	...	Redshift type (<code>spec</code> = spectroscopic, <code>phot</code> = photometric).
<code>redshiftSource</code>	...	Source of the adopted redshift.
<code>M500c</code>	M_{500c}	M_{500} with respect to the critical density, in units of $10^{14} M_{\odot}$. This assumes a scaling relation normalization $10^{A_0} = 3.0 \times 10^{-5}$, which is consistent with recent weak-lensing measurements (Robertson et al. 2024; Shirasaki et al. 2024). Uncertainty column(s): <code>M500c_errPlus</code> , <code>M500c_errMinus</code> .
<code>M200c</code>	M_{200c}	M_{200} with respect to the critical density, in units of $10^{14} M_{\odot}$, converted from M_{500c} using the Bhattacharya et al. (2013) c-M relation. Uncertainty column(s): <code>M200c_errMinus</code> , <code>M200c_errPlus</code> .
<code>M200m</code>	M_{200m}	M_{200} with respect to the mean density, in units of $10^{14} M_{\odot}$, converted from M_{500c} using the Bhattacharya et al. (2013) c-M relation. Uncertainty column(s): <code>M200m_errPlus</code> , <code>M200m_errMinus</code> .

Table A3 — *Continued*

Column	Symbol	Description
M500cUncorr	M_{500c}^{Unc}	M_{500c} in units of $10^{14} M_{\odot}$, uncorrected for bias due to the steepness of the cluster mass function. Uncertainty column(s): M500cUncorr_errPlus, M500cUncorr_errMinus.
A10_M500c	M_{500c}^{A10}	M_{500c}^{A10} in units of $10^{14} M_{\odot}$, assuming the Arnaud et al. (2010) scaling relation (this was the default assumption in previous ACT data releases). Uncertainty column(s): A10_M500c_errPlus, A10_M500c_errMinus.
A10_M200c	...	M_{200} with respect to the critical density, in units of $10^{14} M_{\odot}$, converted from M_{500c}^{A10} using the Bhattacharya et al. (2013) c-M relation. Uncertainty column(s): A10_M200c_errMinus, A10_M200c_errPlus.
A10_M200m	...	M_{200} with respect to the mean density, in units of $10^{14} M_{\odot}$, converted from M_{500c}^{A10} using the Bhattacharya et al. (2013) c-M relation. Uncertainty column(s): A10_M200m_errMinus, A10_M200m_errPlus.
A10_M500cUncorr	...	M_{500c}^{A10} in units of $10^{14} M_{\odot}$, assuming the Arnaud et al. (2010) scaling relation (this was the default assumption in previous ACT data releases), but neglecting the Eddington bias correction. This is the mass estimate to use if you wish to compare with the <i>Planck</i> PSZ2 catalog. Uncertainty column(s): A10_M500cUncorr_errMinus, A10_M500cUncorr_errPlus.
theta500Arcmin	θ_{500c}	Inferred value for the angular size θ_{500c} (arcmin), using the scaling relation model described in Section 2.5. Uncertainty column(s): theta500Arcmin_err.
Q	Q	Value of the filter mismatch function inferred for this cluster (see Section 2.5). Uncertainty column(s): Q_err.
inferred_y_c	y_0	Inferred value for the central Comptonization parameter y_0 ($\times 10^{-4}$), using the scaling relation model described in Section 2.5. Uncertainty column(s): inferred_y_c_err.
inferred_Y500Arcmin2	...	Inferred value for the integrated Comptonization parameter Y_{500c} (arcmin ²). Note that this is a model dependent quantity which depends on the assumed pressure profile and scaling relation parameters, and is not more physically meaningful than using M_{500c} directly. Uncertainty column(s): inferred_Y500Arcmin2_err.
footprint_DES	...	Flag indicating if the cluster falls within the Dark Energy Survey (DES) footprint.
footprint_HSC	...	Flag indicating if the cluster falls within the Hyper Suprime-Cam Subaru Strategic Program (HSC) footprint.
footprint_KiDS	...	Flag indicating if the cluster falls within the Kilo Degree Survey (KiDS) footprint.
footprint_eROSITADe	...	Flag indicating if the cluster falls within the SRG/eROSITA All Sky Survey (eRASS1 Western Galactic hemisphere) footprint.
footprint_Legacy	...	Flag indicating if the cluster falls within the ACT Legacy footprint (see Fig. 2).
zCluster_delta	δ	Density contrast statistic measured at the zCluster photometric redshift. Uncertainty column(s): zCluster_errDelta.
zCluster_source	...	Photometry used for zCluster measurements. One of: DECaLS (DR10), KiDS (DR4), SDSS (DR16), PS1 (DR2).
RM	...	Flag indicating cross-match with a redMaPPer-detected cluster in the SDSS footprint (Rykoff et al. 2014).
eRASS1CL	...	Flag indicating cross-match with an eRASS1 cluster (Bulbul et al. 2024).
RMDES6	...	Flag indicating cross-match with a redMaPPer-detected cluster in the DES Y6 footprint (Rykoff et al. 2016).
WaZP	...	Flag indicating cross-match with a WaZP-detected cluster in the DES Y6 footprint (Benoist et al. 2025).
CAMIRA	...	Flag indicating cross-match with a CAMIRA-detected cluster in the S23B catalog (Oguri et al. 2018 , Oguri et al. in prep.).
MaDCoWS2DR2	...	Flag indicating cross-match with a MaDCoWS DR2 cluster (Thongkham et al. 2024b).
opt_RADeg	...	Alternative optically-determined Right Ascension in decimal degrees (J2000), from a heterogeneous collection of measurements (see opt_positionSource).
opt_decDeg	...	Alternative optically-determined Declination in decimal degrees (J2000), from a heterogeneous collection of measurements (see opt_positionSource).
opt_positionSource	...	Indicates the source of the alternative optically-determined cluster position. CAMIRA (position from the CAMIRA cluster finder; Oguri et al. 2018 , Oguri et al. in prep.), MADCOWS2DR2 (position from MaDCoWS2 DR2; Thongkham et al. 2024b), RM, RMDES6, RMDES6ACT (position from the redMaPPer cluster finder, in SDSS, DES Y3 or Y6; Rykoff et al. 2014, 2016), Vis-BCG (BCG position from visual inspection of available optical/IR imaging; this work and H21), WaZP (position from the WaZP cluster finder in DES Y6; Benoist et al. 2025), WH2015 (position from Wen & Han 2015), WH2022 (position from Wen & Han 2022), WH2024 (position from Wen & Han 2024).
notes	...	If present, at least one of: AGN? (central galaxy may have color or spectrum indicating it may host an AGN); Lensing? (cluster may show strong gravitational lensing features); Merger? (cluster may be a merger); Star formation? (a galaxy near the center may have blue colors which might indicate star formation if it is not a line-of-sight projection). These notes are not comprehensive and merely indicate some systems that were identified as potentially interesting during visual inspection of the available optical/IR imaging.
warnings	...	If present, a warning message related to the redshift measurement for this cluster (e.g., Possible projected system; see Section 3.1).

B. OPTIMIZATION BIAS IN NEMO AND VALIDATION ON END-TO-END SIMULATIONS

To accurately calculate the completeness at low values of \tilde{q} , it is necessary to correct for the optimization bias (e.g., Zubeldia et al. 2021) that results from the use of a matched filter for cluster finding, as in NEMO. This optimization bias arises due to the fact that clusters are identified with peaks in the filtered map, and positive noise fluctuations in the vicinity of a cluster drag the measured cluster location away from the true cluster location. This leads to a small positive bias in the recovered cluster SZ signal (\tilde{y}_0 in our case), which is naturally larger at lower signal-to-noise (\tilde{q}) levels.

We find a model for the optimization bias, and validate the completeness calculation described in Section 2.6, by running NEMO on 30 simulated realizations of the ACT DR6 maps. We construct the simulations as follows. First, we draw random samples in mass and z from the Tinker et al. (2008) HMF over the sky area observed by ACT. SZ signals are assigned to each halo using an assumed scaling relation, including log-normal intrinsic scatter. This produces an initial halo catalog, referred to below as the ‘truth’ catalog. The haloes in this catalog are then randomly placed within the ACT footprint. Pressure profiles are pasted onto these halos following the Arnaud et al. (2010) profile, with angular size set according to the halo mass in the truth catalog, and projected along the line-of-sight to produce a 2D Compton- y map, which is convolved with the appropriate ACT beam for a given frequency channel. At a given frequency we multiply the Compton- y map by tSZ spectral distortion function and T_{CMB} to produce a map of temperature fluctuations from the halos, to which we add simulated CMB (also convolved with the appropriate beam). The final addition to these maps is simulated anisotropic ACT noise, following the inverse variance maps for the real data at each frequency as produced by the map maker (see Naess et al. 2020, 2025). We scale up this white noise by a factor of 1.16 to match the median value of the real DR6 \tilde{y}_0 noise map, since the simulations do not include all possible sources of noise included in the real data. We also add an additional $1/f$ noise component following MacCrann et al. (2024), in order to approximate the impact of the atmosphere.

We process the simulated maps through NEMO, using the same settings as used for the DR6 cluster search (see Section 2.2, except that we do not find and subtract point sources, as these are not included in the simulated maps used here). We cross-match the NEMO output catalogs, which contain measurements of \tilde{y}_0 and \tilde{q} for detected clusters, with the ‘truth’ catalog to assign redshifts.

We calculate the optimization bias by comparing the \tilde{y}_0 outputs recorded in the NEMO output catalogs, to the \tilde{y}_0 values and \tilde{q} values extracted from the output maps produced by NEMO at the known positions of the clusters as recorded in the truth catalog. We refer to the latter as forced photometry measurements, and denote these with the subscript FP in all that follows (i.e., $\tilde{y}_{0\text{FP}}$ and \tilde{q}_{FP} refer to the forced photometry values extracted at true cluster positions from the \tilde{y}_0 and \tilde{q} maps), and use them as proxies for unbiased measurements of the true values of these quantities. A similar approach was used by Zubeldia et al. (2023).

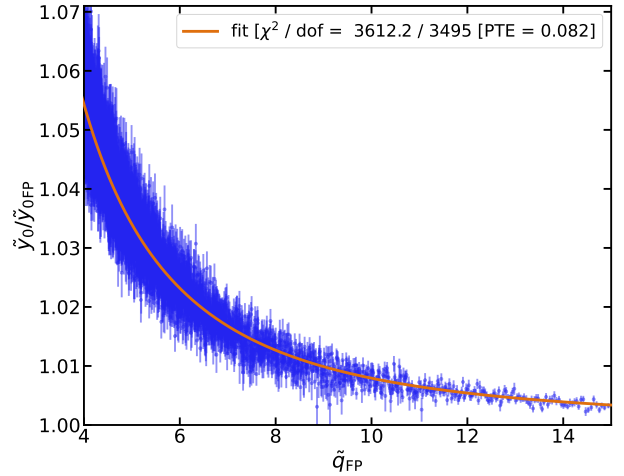


Figure 20. Optimization bias on the extracted SZ signal ($\tilde{y}_0/\tilde{y}_{0\text{FP}}$) as a function of signal-to-noise extracted by forced photometry at true cluster positions (\tilde{q}_{FP}), in a stack of 30 end-to-end simulation runs (the data are binned). The orange line is a fitted model of the form given in Equation B1.

We define the optimization bias to be the ratio $\tilde{y}_0/\tilde{y}_{0\text{FP}}$. In Figure 20 we show this quantity as a function of \tilde{q}_{FP} . We see that there is a clear trend for a larger deviation from 1 (no bias) as \tilde{q}_{FP} decreases, with the bias reaching a value of 1.03 at $\tilde{q}_{\text{FP}} \approx 5$. We model the correction factor C for this bias using

$$C = 1 + \frac{1}{(\tilde{q}_{\text{FP}})^p}, \quad (\text{B1})$$

where $p = 2.1$ is found through fitting the data shown in Figure 20. This value is assumed in the calculations presented in Section 2.6, where we correct the true \tilde{y}_0 predicted from the scaling relation to $\tilde{y}_0^{\text{corr}} = \tilde{y}_0(1 + \frac{1}{\tilde{q}^p})$. Note that Equation B1 diverges for very low values of \tilde{q}_{FP} ; this is handled in the completeness calculations by setting $C = 1$ when \tilde{q} has a value of 3 or more below the chosen \tilde{q}_{cut} value.

We validate the completeness calculations and the optimization bias model by comparing the number of clusters found by NEMO in the simulated maps with predictions that forward model from the Tinker et al. (2008) HMF, using the noise distribution and filter mismatch function as calculated by NEMO. These predictions assume the same cosmology and scaling relation parameters as used to generate the simulated maps. Figure 21 shows the results for all 30 simulation realizations, and their average, evaluated for $\tilde{q}_{\text{cut}} = 5$, within the Legacy footprint. We find that we can accurately predict the number of clusters detected by NEMO as a function of \tilde{q} and z . On average, we detect a total of 5732 $\tilde{q} > 5$ clusters with NEMO, compared to 5766 predicted (i.e., within < 1%, within the Legacy footprint).

The NEMO-SIM-KIT¹² package used to generate the simulated maps, run the NEMO cluster finder, fit the optimization bias model, and produce the validation plots

¹² <https://github.com/simonsobs/nemo-sim-kit>

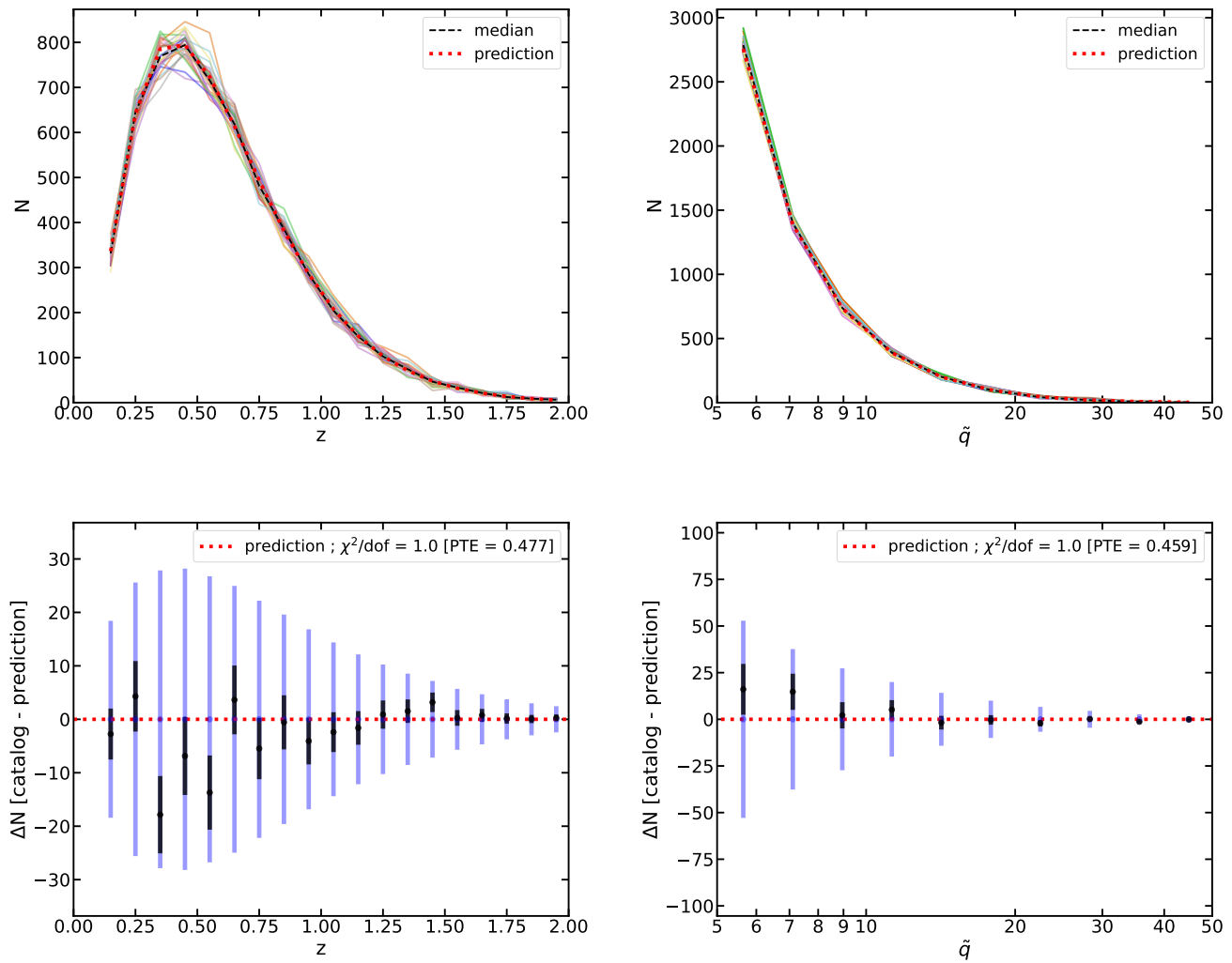


Figure 21. Comparison of the number of $\tilde{q} > 5$ clusters in the Legacy footprint detected by NEMO with forward modeled predictions that use the optimization bias model described in Appendix B and the completeness calculation described in Section 2.6. The top row shows the number of clusters in bins of z (left) and \tilde{q} (right). Different colored lines represent each of the 30 simulation realizations. The dashed black line shows the median number of clusters detected in the simulated maps, while the dashed red line shows the predicted number. The bottom row shows the difference (number of detected clusters minus the prediction), again in bins of z (left) and \tilde{q} (right). The large blue error bars show the $1\text{-}\sigma$ shot noise uncertainty on a single simulation realization, while the black data points with error bars show the average over the 30 simulation realizations. These show that the prediction is well within the accuracy needed to match the number of clusters detected in the DR6-like simulated maps.

shown here, will be made publicly available.

REFERENCES

- Abbott, T. M. C., Adamów, M., Aguena, M., et al. 2021, *ApJS*, **255**, 20
- Adami, C., Giles, P., Koulouridis, E., et al. 2018, *A&A*, **620**, A5
- Ade, P., Aguirre, J., Ahmed, Z., et al. 2019, *J. Cosmology Astropart. Phys.*, **2019**, 056
- Aguena, M., Benoist, C., da Costa, L. N., et al. 2021, *MNRAS*, **502**, 4435
- Ahumada, R., Allende Prieto, C., Almeida, A., et al. 2020, *ApJS*, **249**, 3
- Aihara, H., AlSayyad, Y., Ando, M., et al. 2022, *PASJ*, **74**, 247
- Allen, S. W., Schmidt, R. W., Ebeling, H., Fabian, A. C., & van Speybroeck, L. 2004, *MNRAS*, **353**, 457
- Ansarinejad, B., Murphy, D., Shanks, T., & Metcalfe, N. 2023, *MNRAS*, **520**, 1371
- Archipley, M., Hryciuk, A., Bleem, L. E., et al. 2025, *arXiv e-prints*, [arXiv:2506.00298](https://arxiv.org/abs/2506.00298)
- Arnaud, M., Pratt, G. W., Piffaretti, R., et al. 2010, *A&A*, **517**, A92
- Astropy Collaboration, Robitaille, T. P., Tollerud, E. J., et al. 2013, *A&A*, **558**, A33
- Benoist, C., Aguena, M., da Costa, L., et al. 2025, *arXiv e-prints*, [arXiv:2507.05360](https://arxiv.org/abs/2507.05360)
- Bhattacharya, S., Habib, S., Heitmann, K., & Vikhlinin, A. 2013, *ApJ*, **766**, 32
- Birkinshaw, M. 1999, *Physics Reports*, **310**, 97
- Blake, C., Amon, A., Childress, M., et al. 2016, *MNRAS*, **462**, 4240
- Bleem, L. E., Stalder, B., de Haan, T., et al. 2015, *ApJS*, **216**, 27
- Bleem, L. E., Bocquet, S., Stalder, B., et al. 2020, *ApJS*, **247**, 25
- Bleem, L. E., Klein, M., Abbot, T. M. C., et al. 2024, *The Open Journal of Astrophysics*, **7**, 13
- Bocquet, S., Dietrich, J. P., Schrabback, T., et al. 2019, *ApJ*, **878**, 55
- Bocquet, S., Grandis, S., Bleem, L. E., et al. 2024, *Phys. Rev. D*, **110**, 083510
- Böhringer, H., Voges, W., Huchra, J. P., et al. 2000, *ApJS*, **129**, 435

- Böhringer, H., Schuecker, P., Guzzo, L., et al. 2004, *A&A*, **425**, 367
- Bradley, L. D., Zitrin, A., Coe, D., et al. 2014, *ApJ*, **792**, 76
- Bulbul, E., Liu, A., Kluge, M., et al. 2024, *A&A*, **685**, A106
- Burenin, R. A., Vikhlinin, A., Hornstrup, A., et al. 2007, *ApJS*, **172**, 561
- Calabretta, M. R., & Greisen, E. W. 2002, *A&A*, **395**, 1077
- Carlstrom, J. E., Holder, G. P., & Reese, E. D. 2002, *ARA&A*, **40**, 643
- Cavagnolo, K. W., Donahue, M., Voit, G. M., & Sun, M. 2008, *ApJ*, **682**, 821
- Childress, M. J., Lidman, C., Davis, T. M., et al. 2017, *MNRAS*, **472**, 273
- Chisari, N. E., Alonso, D., Krause, E., et al. 2019, *ApJS*, **242**, 2
- Choi, S. K., Austermann, J., Beall, J. A., et al. 2018, *Journal of Low Temperature Physics*, **193**, 267
- Chon, G., & Böhringer, H. 2012, *A&A*, **538**, A35
- Clerc, N., Kirkpatrick, C. C., Finoguenov, A., et al. 2020, *MNRAS*, **497**, 3976
- Cohn, J. D., Evrard, A. E., White, M., Croton, D., & Ellingson, E. 2007, *MNRAS*, **382**, 1738
- Coziol, R., Andernach, H., Caretta, C. A., Alamo-Martínez, K. A., & Tago, E. 2009, *AJ*, **137**, 4795
- Cruddace, R., Voges, W., Böhringer, H., et al. 2002, *ApJS*, **140**, 239
- De Grandi, S., Böhringer, H., Guzzo, L., et al. 1999, *ApJ*, **514**, 148
- DES Collaboration, Cao, S., Wu, H.-Y., et al. 2025, *arXiv e-prints*, [arXiv:2506.17526](https://arxiv.org/abs/2506.17526)
- DESI Collaboration. 2025, *arXiv e-prints*, [arXiv:2503.14745](https://arxiv.org/abs/2503.14745)
- Dey, A., Schlegel, D. J., Lang, D., et al. 2019, *AJ*, **157**, 168
- Dicker, S. R., Battistelli, E. S., Bhandarkar, T., et al. 2021, *MNRAS*, **508**, 2600
- Dicker, S. R., Perez Sarmiento, K., Mason, B., et al. 2024, *ApJ*, **970**, 84
- Ding, J., Dalal, R., Sunayama, T., et al. 2025, *MNRAS*, **536**, 572
- Eddington, A. S. 1913, *MNRAS*, **73**, 359
- Fassbender, R., Böhringer, H., Santos, J. S., et al. 2011a, *A&A*, **527**, A78
- Fassbender, R., Nastasi, A., Böhringer, H., et al. 2011b, *A&A*, **527**, L10
- Gal, R. R., Lopes, P. A. A., de Carvalho, R. R., et al. 2009, *AJ*, **137**, 2981
- Ghirardini, V., Bulbul, E., Artis, E., et al. 2024, *A&A*, **689**, A298
- Gilbank, D. G., Yee, H. K. C., Ellingson, E., et al. 2008, *ApJL*, **677**, L89
- Gonzalez, A. H., Gettings, D. P., Brodwin, M., et al. 2019, *ApJS*, **240**, 33
- Gralla, M. B., Sharon, K., Gladders, M. D., et al. 2011, *ApJ*, **737**, 74
- Gupta, N., Saro, A., Mohr, J. J., et al. 2017, *MNRAS*, **467**, 3737
- Harrison, I., & Coles, P. 2012, *MNRAS*, **421**, L19
- Hasselfield, M., et al. 2013, *JCAP*, **7**, 8
- Henderson, S. W., Allison, R., Austermann, J., et al. 2016, *Journal of Low Temperature Physics*, **184**, 772
- Hilton, M., Hasselfield, M., Sifón, C., et al. 2018, *ApJS*, **235**, 20
- Hilton, M., Sifón, C., Naess, S., et al. 2021, *ApJS*, **253**, 3
- Hincks, A. D., Acquaviva, V., Ade, P. A. R., et al. 2010, *ApJS*, **191**, 423
- Huang, N., Bleem, L. E., Stalder, B., et al. 2020, *AJ*, **159**, 110
- Isopi, G., Capalbo, V., Hincks, A. D., et al. 2024, *arXiv e-prints*, [arXiv:2410.14404](https://arxiv.org/abs/2410.14404)
- Itoh, N., Kohyama, Y., & Nozawa, S. 1998, *ApJ*, **502**, 7
- Jarrett, T. H., Chester, T., Cutri, R., Schneider, S. E., & Huchra, J. P. 2003, *AJ*, **125**, 525
- Kim, J., Jee, M. J., Hughes, J. P., et al. 2021, *ApJ*, **923**, 101
- Kirkpatrick, C. C., Clerc, N., Finoguenov, A., et al. 2021, *MNRAS*, **503**, 5763
- Klein, M., Hernández-Lang, D., Mohr, J. J., Bocquet, S., & Singh, A. 2023, *MNRAS*, **526**, 3757
- Klein, M., Mohr, J. J., & Davies, C. T. 2024a, *A&A*, **690**, A322
- Klein, M., Mohr, J. J., Bocquet, S., et al. 2024b, *MNRAS*, **531**, 3973
- Kornoelje, K., Bleem, L. E., Rykoff, E. S., et al. 2025, *arXiv e-prints*, [arXiv:2503.17271](https://arxiv.org/abs/2503.17271)
- Krause, E., Pierpaoli, E., Dolag, K., & Borgani, S. 2012, *MNRAS*, **419**, 1766
- Lidman, C., Iacobuta, G., Bauer, A. E., et al. 2013, *MNRAS*, **433**, 825
- Lin, Y.-T., Partridge, B., Pober, J. C., et al. 2009, *ApJ*, **694**, 992
- MacCrann, N., Sherwin, B. D., Qu, F. J., et al. 2024, *ApJ*, **966**, 138
- Mainzer, A., Bauer, J., Grav, T., et al. 2011, *ApJ*, **731**, 53
- Marriage, T. A., et al. 2011, *ApJ*, **737**, 61
- Melin, J. B., Bartlett, J. G., & Delabrouille, J. 2006, *A&A*, **459**, 341
- Menanteau, F., et al. 2010, *ApJ*, **723**, 1523
- , 2012, *ApJ*, **748**, 7
- , 2013a, *ApJ*, **765**, 67
- Menanteau, F., Sifón, C., Barrientos, L. F., et al. 2013b, *ApJ*, **765**, 67
- Merloni, A., Lamer, G., Liu, T., et al. 2024, *A&A*, **682**, A34
- Mortenson, M. J., Hu, W., & Huterer, D. 2011, *Phys. Rev. D*, **83**, 023015
- Mroczkowski, T., Nagai, D., Basu, K., et al. 2019, *Space Sci. Rev.*, **215**, 17
- Mullis, C. R., Rosati, P., Lamer, G., et al. 2005, *ApJL*, **623**, L85
- Mullis, C. R., McNamara, B. R., Quintana, H., et al. 2003, *ApJ*, **594**, 154
- Naess, S., Aiola, S., Austermann, J. E., et al. 2020, *J. Cosmology Astropart. Phys.*, **2020**, 046
- Naess, S., Guan, Y., Duivenvoorden, A. J., et al. 2025, *arXiv e-prints*, [arXiv:2503.14451](https://arxiv.org/abs/2503.14451)
- Nastasi, A., Böhringer, H., Fassbender, R., et al. 2014, *A&A*, **564**, A17
- Newman, A. B., Ellis, R. S., Andreon, S., et al. 2014, *ApJ*, **788**, 51
- Oguri, M. 2014, *MNRAS*, **444**, 147
- Oguri, M., Lin, Y.-T., Lin, S.-C., et al. 2018, *PASJ*, **70**, S20
- Pannuti, T. G., Swartz, D. A., Laine, S., et al. 2015, *AJ*, **150**, 91
- Papovich, C. 2008, *ApJ*, **676**, 206
- Planck Collaboration, Ade, P. A. R., Aghanim, N., et al. 2014, *A&A*, **571**, A29
- , 2015, *A&A*, **581**, A14
- , 2016a, *A&A*, **594**, A24
- , 2016b, *A&A*, **594**, A27
- Poole, G. B., Babul, A., McCarthy, I. G., et al. 2007, *MNRAS*, **380**, 437
- Robertson, N. C., Sifón, C., Asgari, M., et al. 2024, *A&A*, **681**, A87
- Romer, A. K., Nichol, R. C., Holden, B. P., et al. 2000, *ApJS*, **126**, 209
- Rykoff, E. S., Roza, E., Busha, M. T., et al. 2014, *ApJ*, **785**, 104
- Rykoff, E. S., Roza, E., Hollowood, D., et al. 2016, *ApJS*, **224**, 1
- Sahlén, M., Zubeldía, I., & Silk, J. 2016, *ApJL*, **820**, L7
- Sanders, J. S., Fabian, A. C., & Smith, R. K. 2011, *MNRAS*, **410**, 1797
- Santos, J. S., Fassbender, R., Nastasi, A., et al. 2011, *A&A*, **531**, L15
- Sayers, J., Mroczkowski, T., Czakon, N. G., et al. 2013, *ApJ*, **764**, 152
- Scodreggio, M., Guzzo, L., Garilli, B., et al. 2018, *A&A*, **609**, A84
- Shectman, S. A., Landy, S. D., Oemler, A., et al. 1996, *ApJ*, **470**, 172
- Shirasaki, M., Sifón, C., Miyatake, H., et al. 2024, *Phys. Rev. D*, **110**, 103006
- Sifón, C., Battaglia, N., Hasselfield, M., et al. 2016, *MNRAS*, **461**, 248
- Sikhosana, S. P., Hilton, M., Bernardi, G., et al. 2025, *A&A*, **698**, L17
- Simmott, R. W. 1988, NGC 2000.0: The Complete New General Catalogue and Index Catalogues of Nebulae and Star Clusters by J. L. E. Dreyer (Cambridge Univ. Press and Sky Publishing Corporation, Cambridge)
- Smal, I., Ellis, R. S., Dressler, A., et al. 1997, *ApJ*, **479**, 70
- Stanford, S. A., Gonzalez, A. H., Brodwin, M., et al. 2014, *ApJS*, **213**, 25
- Staniszewski, Z., et al. 2009, *ApJ*, **701**, 32
- Stott, J. P., et al. 2010, *ApJ*, **718**, 23
- Struble, M. F., & Rood, H. J. 1991, *ApJS*, **77**, 363
- , 1999, *ApJS*, **125**, 35
- Sunyaev, R., Arefiev, V., Babyshkin, V., et al. 2021, *A&A*, **656**, A132
- Sunyaev, R. A., & Zel'dovich, Y. B. 1970, *Comments on Astrophysics and Space Physics*, **2**, 66

- Sunyaev, R. A., & Zeldovich, Y. B. 1972, *Comments on Astrophysics and Space Physics*, 4, 173
- Swetz, D. S., et al. 2011, *ApJS*, 194, 41
- The Simons Observatory Collaboration, Abitbol, M., Abril-Cabezas, I., et al. 2025, [arXiv e-prints](#), [arXiv:2503.00636](#)
- Thongkham, K., Gonzalez, A. H., Brodwin, M., et al. 2024a, *ApJ*, 967, 123
- . 2024b, *ApJ*, 976, 186
- Thornton, R. J., Ade, P. A. R., Aiola, S., et al. 2016, *ApJS*, 227, 21
- Tinker, J., Kravtsov, A. V., Klypin, A., et al. 2008, *ApJ*, 688, 709
- Valtchanov, I., Pierre, M., Willis, J., et al. 2004, *A&A*, 423, 75
- van Weeren, R. J., de Gasperin, F., Akamatsu, H., et al. 2019, *Space Sci. Rev.*, 215, 16
- Wen, Z. L., & Han, J. L. 2015, *ApJ*, 807, 178
- . 2022, *MNRAS*, 513, 3946
- . 2024, *ApJS*, 272, 39
- Wen, Z. L., Han, J. L., & Liu, F. S. 2012, *ApJS*, 199, 34
- Wik, D. R., Sarazin, C. L., Ricker, P. M., & Randall, S. W. 2008, *ApJ*, 680, 17
- Williamson, R., Benson, B. A., High, F. W., et al. 2011, *ApJ*, 738, 139
- Willis, J. P., Canning, R. E. A., Noordeh, E. S., et al. 2020, *Nature*, 577, 39
- Wright, A. H., Kuijken, K., Hildebrandt, H., et al. 2024, *A&A*, 686, A170
- Wright, E. L., Eisenhardt, P. R. M., Mainzer, A. K., et al. 2010, *AJ*, 140, 1868
- Zhang, Y., Jeltema, T., Hollowood, D. L., et al. 2019, *MNRAS*, 487, 2578
- Zubeldia, Í., Melin, J.-B., Chluba, J., & Battye, R. 2025, *MNRAS*, 539, 185
- Zubeldia, Í., Rotti, A., Chluba, J., & Battye, R. 2021, *MNRAS*, 507, 4852
- . 2023, *MNRAS*, 522, 4766
- OWA, UK
- ²² School of Mathematics and Physics, University of Queensland, Brisbane, QLD 4072, Australia
- ²³ Department of Physics, IIT Hyderabad, Kandi, Telangana 502285, India
- ²⁴ Department of Physics and Astronomy, University of Pennsylvania, 209 South 33rd Street, Philadelphia, PA, USA 19104
- ²⁵ Max-Planck-Institut für Astrophysik, Karl-Schwarzschild-Str. 1, 85748 Garching, Germany
- ²⁶ Department of Astrophysical Sciences, Peyton Hall, Princeton University, Princeton, NJ USA 08544
- ²⁷ Physics Division, Lawrence Berkeley National Laboratory, Berkeley, CA 94720, USA
- ²⁸ Department of Physics, University of California, Berkeley, CA, USA 94720
- ²⁹ Berkeley Center for Cosmological Physics, University of California, Berkeley, CA 94720, USA
- ³⁰ Department of Astronomy and Astrophysics, University of Chicago, Chicago, IL 60637, USA
- ³¹ Kavli Institute for Cosmological Physics, University of Chicago, Chicago, IL 60637, USA
- ³² Institut d'Estudis Espacials de Catalunya (IEEC), 08034 Barcelona, Spain
- ³³ Institute of Space Sciences (ICE, CSIC), Campus UAB, Carrer de Can Magrans, s/n, 08193 Barcelona, Spain
- ³⁴ Department of Aeronautics & Astronautics, Massachusetts Institute of Technology, 77 Mass. Avenue, Cambridge, MA 02139, USA
- ³⁵ Department of Physics, University of Chicago, Chicago, IL 60637, USA
- ³⁶ Center for Astrophysical Surveys, National Center for Supercomputing Applications, 1205 West Clark St., Urbana, IL 61801, USA
- ³⁷ Department of Astronomy, University of Illinois at Urbana-Champaign, 1002 W. Green Street, Urbana, IL 61801, USA
- ³⁸ Department of Physics and Astronomy, University of British Columbia, Vancouver, BC, Canada V6T 1Z4
- ³⁹ Department of Physics, Columbia University, New York, NY 10027, USA
- ⁴⁰ Wits Centre for Astrophysics, School of Physics, University of the Witwatersrand, Private Bag 3, 2050, Johannesburg, South Africa
- ⁴¹ Astrophysics Research Centre, School of Mathematics, Statistics and Computer Science, University of KwaZulu-Natal, Durban 4001, South Africa

AFFILIATIONS

¹ INAF-Osservatorio Astronomico di Trieste, via G. B. Tiepolo 11, I-34143 Trieste, Italy

² Laboratório Interinstitucional de e-Astronomia - LIneA, Av. Pastor Martin Luther King Jr, 126 Del Castilho, Nova América Offices, Torre 3000/sala 817 CEP: 20765-000, Brazil

³ Flatiron Institute, 162 5th Avenue, New York, NY 10010 USA

⁴ Joseph Henry Laboratories of Physics, Jadwin Hall, Princeton University, Princeton, NJ, USA 08544

⁵ Fermi National Accelerator Laboratory, P. O. Box 500, Batavia, IL 60510, USA

⁶ Physik-Institut, University of Zürich, Winterthurerstrasse 190, CH-8057 Zürich, Switzerland

⁷ Institute of Cosmology and Gravitation, University of Portsmouth, Portsmouth, PO1 3FX, UK

⁸ Department of Astrophysical Sciences, Peyton Hall, Princeton University, Princeton, New Jersey 08544, USA

⁹ Department of Astronomy, Cornell University, Ithaca, NY 14853, USA

¹⁰ Sapienza University of Rome, Physics Department, Piazzale Aldo Moro 5, 00185 Rome, Italy

¹¹ University Observatory, LMU Faculty of Physics, Scheinerstr. 1, 81679 Munich, Germany

¹² Department of Physics, Madingley Road, Cambridge CB3 0HA, UK

¹³ Kavli Institute for Cosmology Cambridge, Madingley Road, Cambridge CB3 0HA, UK

¹⁴ Canadian Institute for Theoretical Astrophysics, University of Toronto, Toronto, ON, Canada M5S 3H8

¹⁵ Department of Physics & Astronomy, University College London, Gower Street, London, WC1E 6BT, UK

¹⁶ School of Physics and Astronomy, Cardiff University, The Parade, Cardiff, Wales, UK CF24 3AA

¹⁷ Institut de Física d'Altes Energies (IFAE), The Barcelona Institute of Science and Technology, Campus UAB, 08193 Bellaterra (Barcelona) Spain

¹⁸ Department of Physics and Astronomy, University of California, Riverside, CA 92521, USA

¹⁹ Astronomy Unit, Department of Physics, University of Trieste, via Tiepolo 11, I-34131 Trieste, Italy

²⁰ Institute for Fundamental Physics of the Universe, Via Beirut 2, 34014 Trieste, Italy

²¹ DAMTP, Centre for Mathematical Sciences, University of Cambridge, Wilberforce Road, Cambridge CB3

- ⁴² David A. Dunlap Dept of Astronomy and Astrophysics, University of Toronto, 50 St George Street, Toronto ON, M5S 3H4, Canada
- ⁴³ Specola Vaticana (Vatican Observatory), V-00120 Vatican City State
- ⁴⁴ Santa Cruz Institute for Particle Physics, Santa Cruz, CA 95064, USA
- ⁴⁵ Center for Cosmology and Astro-Particle Physics, The Ohio State University, Columbus, OH 43210, USA
- ⁴⁶ Department of Physics, The Ohio State University, Columbus, OH 43210, USA
- ⁴⁷ NIST Quantum Sensors Group, 325 Broadway Mailcode 817.03, Boulder, CO, USA 80305
- ⁴⁸ Mitchell Institute for Fundamental Physics & Astronomy and Department of Physics & Astronomy, Texas A&M University, College Station, Texas 77843, USA
- ⁴⁹ Department of Physics and Astronomy, Rutgers, The State University of New Jersey, Piscataway, NJ USA 08854-8019
- ⁵⁰ Center for Astrophysics | Harvard & Smithsonian, 60 Garden Street, Cambridge, MA 02138, USA
- ⁵¹ Centre for Radio Astronomy Techniques and Technologies, Department of Physics and Electronics, Rhodes University, P.O. Box 94, Makhanda 6140, South Africa
- ⁵² Department of Physics, Yale University, 217 Prospect St, New Haven, CT 06511
- ⁵³ Department of Physics and Astronomy, University of Pittsburgh, Pittsburgh, PA, USA 15260
- ⁵⁴ Institute of Astronomy and Astrophysics, Academia Sinica, Taipei 10617, Taiwan; Institute of Physics, National Yang Ming Chiao Tung University, Hsinchu 30010, Taiwan
- ⁵⁵ Institut de Física d'Altes Energies (IFAE), The Barcelona Institute of Science and Technology, Campus UAB, 08193 Bellaterra, Spain
- ⁵⁶ Kavli Institute for Particle Astrophysics & Cosmology, P. O. Box 2450, Stanford University, Stanford, CA 94305, USA
- ⁵⁷ SLAC National Accelerator Laboratory, Menlo Park, CA 94025, USA
- ⁵⁸ Leiden Observatory, Leiden University, P.O. Box 9513, 2300 RA Leiden, The Netherlands
- ⁵⁹ George P. and Cynthia Woods Mitchell Institute for Fundamental Physics and Astronomy, and Department of Physics and Astronomy, Texas A&M University, College Station, TX 77843, USA
- ⁶⁰ Kavli Institute for Cosmological Physics, University of Chicago, 5640 S. Ellis Ave., Chicago, IL 60637, USA
- ⁶¹ Department of Astronomy and Astrophysics, University of Chicago, 5640 S. Ellis Ave., Chicago, IL 60637, USA
- ⁶² Enrico Fermi Institute, University of Chicago, Chicago, IL 60637, USA
- ⁶³ Université Grenoble Alpes, CNRS, LPSC-IN2P3, 38000 Grenoble, France
- ⁶⁴ Institució Catalana de Recerca i Estudis Avançats, E-08010 Barcelona, Spain
- ⁶⁵ Kobayashi-Maskawa Institute for the Origin of Particles and the Universe (KMI), Nagoya University, Furo-cho, Chikusa-ward, Nagoya, Aichi, 464-8602, Japan
- ⁶⁶ Institute for Advanced Research, Nagoya University, Furo-cho, Chikusa-ward, Nagoya, Aichi, 464-8601, Japan
- ⁶⁷ Kavli Institute for the Physics and Mathematics of the Universe (WPI), University of Tokyo, 5-1-5, Kashiwa-no-ha, Kashiwa, Chiba, 277-8583, Japan
- ⁶⁸ European Southern Observatory, Karl-Schwarzschild-Str. 2, D-85748, Garching, Germany
- ⁶⁹ Institute of Theoretical Astrophysics, University of Oslo, Norway
- ⁷⁰ Department of Physics, University of Milano - Bicocca, Piazza della Scienza, 3 - 20126, Milano (MI), Italy
- ⁷¹ Jodrell Bank Centre for Astrophysics, Department of Physics and Astronomy, The University of Manchester, Manchester M13 9PL, UK
- ⁷² Department of Physics, Cornell University, Ithaca, NY, USA 14853
- ⁷³ Centro de Tecnologia da Informação Renato Archer, Campinas, SP, Brazil - 13069-901
- ⁷⁴ Observatório Nacional, Rio de Janeiro, RJ, Brazil - 20921-400
- ⁷⁵ Center for Frontier Science, Chiba University, Chiba 263-8522, Japan
- ⁷⁶ Department of Physics, Graduate School of Science, Chiba University, Chiba 263-8522, Japan
- ⁷⁷ Department of Physics and Astronomy, Haverford College, Haverford, PA, USA 19041
- ⁷⁸ Hamburger Sternwarte, Universität Hamburg, Gojenbergsweg 112, 21029 Hamburg, Germany
- ⁷⁹ Centro de Investigaciones Energéticas, Medioambientales y Tecnológicas (CIEMAT), Madrid, Spain
- ⁸⁰ Ruhr University Bochum, Faculty of Physics and Astronomy, Astronomical Institute, German Centre for Cosmological Lensing, 44780 Bochum, Germany
- ⁸¹ Department of Physics, Stanford University, Stanford, CA 94305-4085, USA
- ⁸² Kavli Institute for Particle Astrophysics and Cosmology, 382 Via Pueblo Mall Stanford, CA 94305-4060, USA
- ⁸³ SLAC National Accelerator Laboratory 2575 Sand Hill Road Menlo Park, California 94025, USA
- ⁸⁴ Department of Physics and Astronomy, Pevensey Building, University of Sussex, Brighton, BN1 9QH, UK
- ⁸⁵ Instituto de Astrofísica de Canarias, E-38205 La Laguna, Tenerife, Spain
- ⁸⁶ Universidad de La Laguna, Dpto. Astrofísica, E-38206 La Laguna, Tenerife, Spain
- ⁸⁷ Department of Physics, Northeastern University, Boston, MA 02115, USA
- ⁸⁸ Instituto de Física, Pontificia Universidad Católica de Valparaíso, Casilla 4059, Valparaíso, Chile
- ⁸⁹ Physics Department, Lancaster University, Lancaster, LA1 4YB, UK
- ⁹⁰ Computer Science and Mathematics Division, Oak Ridge National Laboratory, Oak Ridge, TN 37831
- ⁹¹ Department of Physics, Duke University, Durham, NC, 27708, USA
- ⁹² Department of Astronomy, University of California, Berkeley, 501 Campbell Hall, Berkeley, CA 94720, USA
- ⁹³ Lawrence Berkeley National Laboratory, 1 Cyclotron Road, Berkeley, CA 94720, USA
- ⁹⁴ Max Planck Institute for Extraterrestrial Physics, Giessenbachstrasse, 85748 Garching, Germany
- ⁹⁵ Universitäts-Sternwarte, Fakultät für Physik, Ludwig-Maximilians Universität München, Scheinerstr. 1, 81679 München, Germany
- ⁹⁶ NASA/Goddard Space Flight Center, Greenbelt,

MD, USA 20771

⁹⁷ Institute of Astronomy, Madingley Road, Cambridge
CB3 0HA, UK

This paper was built using the Open Journal of As-

trophysics L^AT_EX template. The OJA is a journal which provides fast and easy peer review for new papers in the **astro-ph** section of the arXiv, making the reviewing process simpler for authors and referees alike. Learn more at <http://astro.theoj.org>.